



저작자표시-비영리-동일조건변경허락 2.0 대한민국

이용자는 아래의 조건을 따르는 경우에 한하여 자유롭게

- 이 저작물을 복제, 배포, 전송, 전시, 공연 및 방송할 수 있습니다.
- 이차적 저작물을 작성할 수 있습니다.

다음과 같은 조건을 따라야 합니다:



저작자표시. 귀하는 원저작자를 표시하여야 합니다.



비영리. 귀하는 이 저작물을 영리 목적으로 이용할 수 없습니다.



동일조건변경허락. 귀하가 이 저작물을 개작, 변형 또는 가공했을 경우에는, 이 저작물과 동일한 이용허락조건하에서만 배포할 수 있습니다.

- 귀하는, 이 저작물의 재이용이나 배포의 경우, 이 저작물에 적용된 이용허락조건을 명확하게 나타내어야 합니다.
- 저작권자로부터 별도의 허가를 받으면 이러한 조건들은 적용되지 않습니다.

저작권법에 따른 이용자의 권리는 위의 내용에 의하여 영향을 받지 않습니다.

이것은 [이용허락규약\(Legal Code\)](#)을 이해하기 쉽게 요약한 것입니다.

[Disclaimer](#)

Doctor of Philosophy

**Enhancement of Photocatalysis of TiO₂ by
EDTA-assisted Sol-Gel Synthesis for Removal
of Organic Pollutants from Aqueous Solution
under Visible Light Irradiation**

**The Graduate School
of the University of Ulsan**

**Department of Civil and
Environmental Engineering
Nguyen - Le, Minh - Tri**

**Enhancement of Photocatalysis of TiO₂ by
EDTA-assisted Sol-Gel Synthesis for Removal
of Organic Pollutants from Aqueous Solution
under Visible Light Irradiation**

Supervisor: Professor Lee, Byeong – Kyu

A Dissertation

Submitted to

the Graduate School of the University of Ulsan

In partial Fulfillment of the Requirements

for the Degree of

Doctor of Philosophy

by

Nguyen - Le, Minh - Tri

Department of Civil and Environmental Engineering

Ulsan, Korea

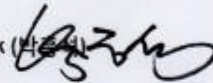
February, 2018

**Enhancement of Photocatalysis of TiO₂ by
EDTA-assisted Sol-Gel Synthesis for Removal
of Organic Pollutants from Aqueous Solution
under Visible Light Irradiation**

This certifies that the dissertation
of Nguyen - Le, Minh - Tri is approved.

Committee Chair:

Prof. Park, Hung - Suck (박흥석)



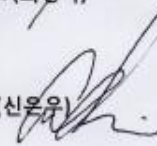
Committee Member:

Prof. Choi, Sung - Deuk (최성득)



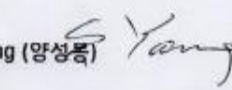
Committee Member:

Prof. Shin, Eun - Woo (신은우)



Committee Member:

Prof. Yang, Sung - Bong (양성봉)



Committee Member:

Prof. Lee, Byeong - Kyu (이병규)



Department of Civil and Environmental Engineering

Ulsan, Korea

February, 2018

ACKNOWLEDGEMENTS

“We can’t solve problems by using the same kind of thinking we used when we created them.”

Albert Einstein

I have learnt such a good lesson since I started my Ph.D. project. I had to confront with many tough questions at the first stages of my project. However, thank God, I finally solved them! At the precise moment in time, I am still wondering how I could complete my project better than I had expected. Frankly, this was my first experience working on a research paper and I would not be able to complete it on time without the help and support of others. Therefore, I would like to show my sincere gratefulness to those who supported me not only for financial aid but for mental inspiration also.

Firstly, I would like to thank my advisor, Prof. Byeong-Kyu Lee, for his valuable guidance and on-time feedback. Without his kindly help and continuous support, I could not finish my project on time. Secondly, I would like to thank the committee members, Prof. Hung-Suck Park (Chairman), Prof. Sung-Bong Yang, Prof. Sung-Deuk Choi and Prof. Eun-Woo Shin, for their valuable and positive feedback on my paper writing. Such evaluation helps to improve the quality of my dissertation. Thirdly, I would like to thank the Air Environmental and Energy Research Lab current members and our alumni for their kindly assistance not only during the project process but also during my settlement in Korea. Last but not least, I especially would like to show my gratefulness to my beloved family and my best friends in Korea and Vietnam for their encouragement whenever I felt a bit down during this project trajectory. You are my motivation for keeping moving forward.

Ulsan, November 04th, 2017

Nguyen Le Minh Tri

PUBLICATION

Peer-reviewed Journals

1/ *Effective photodegradation of dyes using in-situ N-Ti³⁺ co-doped porous titanate-TiO₂ rod-like heterojunctions*, M.T. Nguyen-Le, B.K. Lee, **Catalysis Today**, 297, 228-236, 2017. (IF = 4.6)

2/ *EDTA-Na₂-assisted synthesis of rod-like titanate-TiO₂ composite architectures with enhanced visible-light-driven properties*, M.T. Nguyen-Le, B.K. Lee, D.M. Tran, **Journal of Industrial and Engineering Chemistry**, 56, 225-233, 2017. (IF = 4.4)

3/ *Novel fabrication of a nitrogen-doped mesoporous TiO₂-nanorod titanate heterojunction to enhance the photocatalytic degradation of dyes under visible light*, M.T. Nguyen-Le, B.K. Lee, **RSC Advances**, 6, 31347-31350, 2016. (IF = 3.1)

4/ *High temperature synthesis of interfacial functionalized carboxylate mesoporous TiO₂ for effective adsorption of cationic dyes*, M.T. Nguyen-Le, B.K. Lee, **Chemical Engineering Journal**, 281, 20-33, 2015. (IF = 6.2)

Conference Proceedings

1/ *Facile synthesis of structure engineered nanorod titanate-TiO₂ composite and its photocatalytic performance under visible light*, M.T. Nguyen-Le, B.K. Lee. International Conference on Green Technologies for Sustainable Water, Vietnam, 2017 (Oral)

2/ *Effective photodegradation of dyes using in-situ N-Ti³⁺ codoped porous*

titanate-TiO₂ rod-like heterojunctions. M.T. Nguyen-Le, B.K. Lee. The 2nd international symposium on Catalytic Science and Technology in Sustainable Energy and Environment, China, 2016 (Oral)

3/ *Enhanced removal of methylene blue onto interfacial functionalized mesoporous TiO₂ from aqueous solution by adsorption and photocatalysis*. M.T. Nguyen-Le, B.K. Lee. The 1st international water nexus conference, Korea, 2015 (Poster).

4/ *Comparison of characteristics of 16 PAHs in road dust from two largest cities of Vietnam*. M.T. Nguyen-Le, B.K. Lee. The 58th Korean Society for Atmospheric Environment Conference, Korea, 2015 (Poster).

5/ *Removal of cationic dyes from wastewater using a mesoporous modified TiO₂-based adsorbent*. M.T. Nguyen-Le, B.K. Lee. The 2nd International Young Researchers Workshop on River Basin Environment and Management, Vietnam, 2015 (Oral).

6/ *Removal of methylene blue dye from aqueous solution using a high surface area mesoporous TiO₂: Equilibrium, kinetics and thermodynamics*. M.T. Nguyen-Le, B.K. Lee. The 57th Korean Society for Atmospheric Environment Conference, Korea, 2014 (Poster).

7/ *Toxicity and source apportionment of PAHs in road dust from Hanoi and Ho Chi Minh City, Vietnam*. M.T. Nguyen-Le, B.K. Lee. International Aerosol Conference, Korea, 2014 (Poster).

8/ *The potential application of a mesoporous modified TiO₂-based adsorbent for removal of methylene blue dye from aqueous solution*. M.T. Nguyen-Le, B.K. Lee.

The 8th International Conference/ Exhibition on Combustion, Incineration/ Pyrolysis, Emission and Climate Change, China, 2014 (Oral).

9/ Removal of Cd (II) from aqueous solution by biochar-Alginate capsule. X.H. Do, M.V. Nguyen, M.T. Nguyen-Le, J.T. Kim, D.W. Lee, B.K. Lee. The 30th Korean Society for Atmospheric Environment Conference, Korea, 2014 (Poster).

CONTENTS

ABSTRACT	1
CHAPTER 1. INTRODUCTION	2
1.1. Research Purpose and Scope	2
1.2. Research Outline.....	4
CHAPTER 2. LITERATURE REVIEW	5
2.1. Titanium dioxide (TiO ₂)	5
2.1.1. History background	5
2.1.2. TiO ₂ structure and properties	11
2.2. Strategies for enhance TiO ₂ photocatalytic activity	15
2.2.1. Morphological modification	15
2.2.2. Chemical modification.....	17
2.2.3. Sensitization of TiO ₂	19
2.3. Application.....	19
2.4. Mesoporous materials.....	21
2.4.1. Definition and classification	21
2.4.2. Application of mesoporous materials.....	23
2.5. Sol-gel method	24
2.5.1. Overview.....	24
2.5.2. Contributing factors in sol-gel process.....	25
2.5.3. Advantages and drawbacks of the sol-gel method.....	29
2.6. Dyes and treatment methods	30
2.6.1. Classification of dyes.....	30
2.6.2. Toxicity of dyes	32
2.6.3. Dye treatment methods	32

CHAPTER 3. EDTA-NA₂-ASSISTED SYNTHESIS OF ROD-LIKE TITANATE-TIO₂ COMPOSITE ARCHITECTURES35

3.1. Preparation of the composite35

3.1.1. Chemicals.....35

3.1.2. Preparation of photocatalysts.36

3.1.3. Characterization.....36

3.2. Photocatalytic activity test.....37

3.3. Results and discussion39

3.3.1. Material properties.....39

3.3.2. The role of EDTA-NA₂.....52

3.3.3. Visible light photocatalytic activity53

3.4. Conclusions.....59

CHAPTER 4. EFFECT OF CALCINATION TEMPERATURE ON THE VISIBLE-LIGHT DRIVEN PHOTOCATALYTIC PERFORMANCE OF TITANATE-TIO₂ COMPOSITES.....60

4.1. Preparation of the composite61

4.1.1. Chemicals.....61

4.1.2. Preparation method.....61

4.1.3. Characterization.....61

4.2. Photocatalytic activity test.....63

4.3. Results and discussion63

4.3.1. Effects of calcination temperature on the physical properties of TiO₂-BTs63

4.3.2. Effects of calcination temperature on the photocatalytic activity of TiO₂-BTs under visible light.73

4.4. Conclusions.....74

CHAPTER 5. CONCLUSION AND FUTURE STUDY PLAN76

REFERENCESi

LIST OF TABLES

Table 1: Classification of dyes in term of chemical structure.....	30
Table 2: Classification of dyes according to method of application.....	31
Table 3: Advantages and disadvantages of different dye removal methods.....	32
Table 4: Surface area, pore diameter, pore volume, nitrogen content, and band gap of the modified samples and pristine TiO₂.....	46
Table 5: Surface area, pore diameter, pore volume, nitrogen content and bandgap of TiO₂-400 and TiO₂-BTs.....	66

LIST OF FIGURES

Figure 2-1: Schematic of the chloride process.....	6
Figure 2-2: Diagram of photo-electrochemical cell.....	7
Figure 2-3: Effect of the UV exposure on the contact angle of TiO ₂ surface	9
Figure 2-4: The schematic illustration of transformation of the superficial OH groups under UV and in dark.....	10
Figure 2-5: Mechanism of E.coli disinfection for the copper doped TiO ₂ material under weak UV light	11
Figure 2-6: Crystalline structures of titanium dioxide	12
Figure 2-7: Schematic illustration of the photoexcitation and charge-carrier recombination in TiO ₂ photocatalyst.....	13
Figure 2-8: Classification of porous materials in respect to pore size	21
Figure 2-9: The IUPAC classification of adsorption - desorption isotherms	22
Figure 2-10: Scheme of sol-gel reaction	25
Figure 2-11: Hydrolysis mechanism of an alkoxy silane using acidic catalyst.....	26
Figure 2-12: Condensation mechanism of an alkoxy silane using acidic catalyst.....	27
Figure 2-13: Mechanism of an alkoxy silane using basic catalyst.	28
Figure 3-1. Schematic diagram of the photocatalytic reactor.....	38
Figure 3-2. XRD and Raman spectra of x at % EDTA-Na ₂ /TiO ₂ and pristine TiO ₂	39

Figure 3-3. FTIR spectra of pristine TiO₂ and x at % EDTA-Na₂/TiO₂ (x = 0.5, 1.0, 1.5) obtained at 400 °C. FTIR spectra of xerogel pristine TiO₂ and xerogel 0.5 at % EDTA-Na₂/TiO₂.....	41
Figure 3-4. FE-SEM of the pristine TiO₂ and 0.5, 1.0, 1.5 at % EDTA-Na₂/TiO₂, respectively. EDX of the pristine TiO₂ and 1.0 at % EDTA-Na₂/TiO₂.	44
Figure 3-5. SEM mapping images of 1.0 at % EDTA-Na₂/TiO₂ with the elements of Ti, O, N, C, Na.....	45
Figure 3-6. Nitrogen adsorption-desorption isotherms and pore size distribution of x at % EDTA-Na₂/TiO₂ (x = 0.5, 1.0, 1.5) and pristine TiO₂.....	47
Figure 3-7. XPS spectra details for Ti 2p level of x at % EDTA-Na₂/TiO₂ and pristine TiO₂.	48
Figure 3-8. XPS spectra details for O 1s level and C 1s level of x at % EDTA-Na₂/TiO₂ and pristine TiO₂.....	49
Figure 3-9. XPS spectra details for N 1s level of 1.0 at % EDTA-Na₂/TiO₂.....	50
Figure 3-10. UV-vis spectra of the pristine and modified samples.....	51
Figure 3-11. Visible light photocatalytic degradation of 20 mL of 10 mg/L MB.	54
Figure 3-12. Kinetic curves and reaction rate constants for MB degradation over the as-prepared photocatalysts	55
Figure 3-13. PL spectra of pristine and EDTA-Na₂-modified samples with an excitation wavelength of 325 nm	56
Figure 3-14. MB photocatalytic degradation of 1.0 at % EDTA-Na₂/TiO₂ in the presence of different scavengers.....	57

Figure 4-1. FE-SEM images of TiO₂-400 and TiO₂-BT-400, 600, 800, respectively	64
Figure 4-2. XRD patterns of TiO₂-400 and TiO₂-BTs.	65
Figure 4-3. Nitrogen adsorption-desorption isotherms of TiO₂-400 and TiO₂-BTs	67
Figure 4-4. XPS spectra details for C 1s level and O 1s level of TiO₂-400 and TiO₂-BTs.....	68
Figure 4-5. XPS spectra details for N 1s level of TiO₂-BT-400.....	69
Figure 4-6. XPS spectra details for Ti 2p level of TiO₂-400 and TiO₂-BTs	71
Figure 4-7. UV-vis spectra and Kubelka – Munk plots of TiO₂-400 and TiO₂-BTs.....	72
Figure 4-8. Photocatalytic degradation of 20 mL of 10 mg/L MB under visible light in 2 h by using 20 mg of TiO₂-400 and TiO₂-BTs	73

ABSTRACT

In this study, a simple EDTA- Na_2 assisted - sol-gel approach was applied to fabricate novel N- Ti^{3+} co-doped porous titanate- TiO_2 rod-like heterostructures with both enhanced adsorption ability and visible light photocatalytic activity. EDTA- Na_2 was found to alter the condensation pathway of the titanium precursor. This study also identified the different loading effects of EDTA- Na_2 on the adsorption and photocatalytic degradation. The heterostructure with 1.0 at. % loading of EDTA- Na_2 exhibited moderate adsorption ability, but high photocatalytic activity, which was attributed to the low recombination rate of photo-induced charge carriers. We also investigated the effect of calcination temperature on the physical properties and visible light photocatalytic activity of the heterostructures. When calcined at high temperature ($> 400\text{ }^\circ\text{C}$), the rod-like heterostructures became thermally less stable due to the structural conversion of the visible-light-active composite ($\text{Na}_2\text{Ti}_3\text{O}_7$ – anatase rod-like heterostructures) into the visible-light-inactive form ($\text{Na}_2\text{Ti}_3\text{O}_7$ - $\text{Na}_2\text{Ti}_6\text{O}_{13}$ heterostructures). High mesoporosity, low recombination rate of electrons and holes, and effective incorporation of nitrogen dopants and Ti^{3+} defects were the main features of the enhanced photocatalytic activity of the rod-like heterostructures in the degradation of methylene blue (MB) under visible light. $\cdot\text{O}_2^-$ was the dominated radical for MB photodegradation.

CHAPTER 1. INTRODUCTION

1.1. Research Purpose and Scope

Over the past several decades, photocatalytic oxidation processes have become regarded as effective methods for the decomposition of pollutants, particularly dyes in wastewater. A variety of semiconductors have been utilized as the photocatalysts such as TiO_2 , V_2O_5 , WO_3 and ZnO [1]. In case of photocatalytic semiconductors, TiO_2 is generally accepted as the most effective photocatalyst for decomposition of different organic dyes due to its strong oxidative power and long-term photo-stability.[2] TiO_2 is also inexpensive and safe for water treatment. Unfortunately, TiO_2 has wide band gap energy which can hinder its photocatalytic activity by absorbing only ultraviolet (UV) light irradiation. The visible light utilization of TiO_2 for removal dyes is extremely low. Various strategies, including the doping TiO_2 with other metals and non-metals, and the fabrication of TiO_2 composites, have been applied to overcome these limitations of TiO_2 [3]. The use of metal dopants exhibited several drawbacks such as less thermal stability, lower mobility and higher recombination of photoinduced carriers than other methods [4]. Alternatively, doping TiO_2 with non-metals has been made to extent the photoresponse of TiO_2 from the UV to the visible light region. Among non-metal doping, nitrogen doping is more feasible and effective due to the chemical stability, metastable center formation, small ionization energy and comparable atomic size with oxygen [4].

Coupling TiO_2 with alkali-metal titanates ($\text{A}_2\text{Ti}_n\text{O}_{2n+1}$, where A is Li, Na or K and $n = 3 - 8$), which have an edge-sharing TiO_6 octahedral layered structure ($n = 3 - 4$) or

tunnel structure is another way to enhance the visible light harvesting of TiO₂. Several studies on the synthesis of titanate-TiO₂ hybrids for advanced applications have been documented [5]. However, most of the synthesis were conducted in a high alkali media or need organic solvents for post-treatment to obtain final products. To the best of our knowledge, little efforts focus on the work for the synthesis of nanorod titanate-TiO₂ hybrids via a “green” and alkali-free method using EDTA-Na₂ as both template-directed modifier and nitrogen source.

Ethylenediaminetetraacetic acid (EDTA) has been widely used in many industries as a chelating agent due to its ability to form a stable complex with alkali metals, rare earth elements and transition metals in aqueous solution [6]. In case of inorganic material synthesis, EDTA is often used as a template-directed modifier. Zhang et al. succeeded in the synthesis of Fe₃O₄ octahedrons using EDTA under mild conditions [7]. The synthesis of β-NaLuF₄ in the presence of ethylenediaminetetraacetic disodium salt (EDTA-Na₂) as an additive under hydrothermal treatment and post-washing process was reported by Li et al [8]. Moreover, urchin-like LaVO₄:Eu nanocrystals were also fabricated by the hydrothermal method with the aid of EDTA.[9] EDTA is also well-known as a nitrogen source to achieve visible-light-driven nitrogen doping photocatalysts [10].

In this work, we provide a simple fabrication of visible-light-driven titanate-TiO₂ rod-like composites through a EDTA-Na₂-assisted route for removal of organic pollutants in aqueous solution.

1.2. Research Outline

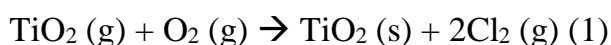
- Synthesis of novel N-Ti³⁺ co-doped porous titanate-TiO₂ rod-like heterostructures.
- Characterization of as-synthesized materials.
- Evaluation of adsorption ability and photocatalytic activity of the photocatalysts via the degradation of Methylene blue dye.
- Investigation of the influence of the calcination temperature on the physical properties and photocatalytic activity of TiO₂-titanate heterostructures.
- Study of removal mechanisms

CHAPTER 2. LITERATURE REVIEW

2.1. Titanium dioxide (TiO₂)

2.1.1. History background

TiO₂ has been introduced to the public as a white pigment since 1916. The white color of TiO₂ is due to its no absorption in the visible region. Ancient people mostly used TiO₂ as a pigment for paints, plastic and paper. Most TiO₂ were made by the so-called “sulfate” process. In this process, TiO₂ derived from the Ilmentile ore is dissolved in sulfuric acid (H₂SO₄), followed by precipitation and separation of iron sulfate (FeSO₄) from the liquid titanium sulfate [Ti(SO₄)₂] under heating to decompose and precipitates out TiO₂. This method, however, was costly at that time, which initially prevented TiO₂ from the widespread use. Another method to produce TiO₂ more economically is the so-called “chloride” process which was initially discovered as early as 1928 and has been developed by many manufacturers later. The developed process involves the Ilmentile ore chlorination, distillation of titanium tetrachloride (TiCl₄) and oxidation of the TiCl₄ vapor at high temperature (Fig.2-1). Pure TiCl₄ made by the chlorination of Ilmenite ore is purified by distillation and fed to the flame reactor (oxidizer) at 1,000 – 1,500°C. Most TiO₂ (about 200 nm) is then produced and introduced to a series of wet processes (finishing) to be suspended in paints while by-product Cl₂ is recycled for the ore chlorination. TiO₂ powders are obtained from the TiCl₄ vapor via the following reaction:



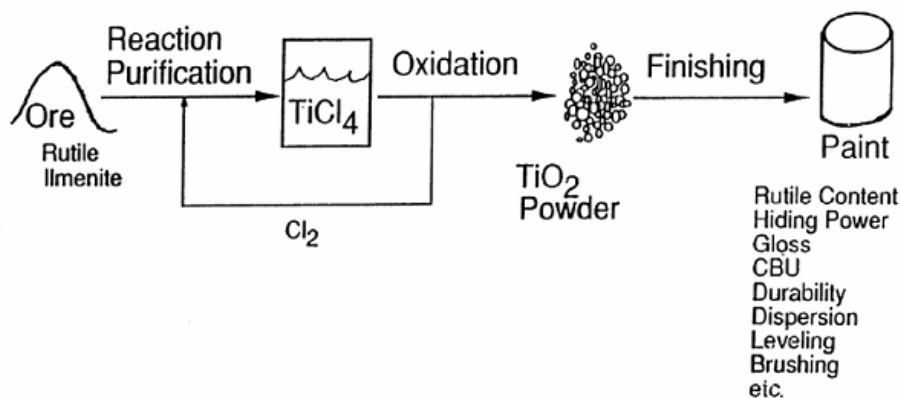


Figure 2-1: Schematic of the chloride process [11].

The discovery of the chloride process has made TiO₂ become widespread and inexpensive. However, TiO₂ has been found to be chemically stable only in dark. Instead, it is active under UV light or even sunlight, which is composed of 3 % of UV irradiation. Such unstable state of TiO₂ under sunlight was pointed out from the flaking of paints and the degradation of fabrics made of TiO₂ [12]. Therefore, TiO₂ has been believed to be effective for the degradability of pollutants under UV irradiation since ancient times. Some scientific reports on the photocatalytic activity of TiO₂ for the removal of pollutants have been conducted since the early 20th century. However, the beauty of this photoactivity of TiO₂ got a limited scientists' attraction, only in the field of either of photocatalyst or photochemistry. Moreover, the "photocatalyst" terminology was not widely used in academic field. The "photosensitizer" terminology was used instead.

In 1972, Honda and Fujishima discovered the photocatalytic splitting of water in TiO₂ electrodes, followed by both the photocatalytic cleaning effect and the photocatalytic antibacterial effect of TiO₂ incorporated materials in early 1990s. This breakthrough invention marked the beginning of a new era in heterogenous

photocatalysis. Since then, many researches on the enhancement of the photocatalytic efficiency of TiO_2 have been carried out by physicists, chemists and engineers.

2.1.1.1. Photocatalytic splitting of water with TiO_2 electrode

In 1960s, Honda and Fujishima conducted the water photolysis under solar radiation, using a single crystal n-type TiO_2 electrode, whose electrode potential of valence band is more positive than that of $\text{O}_2/\text{H}_2\text{O}$ redox pair. The photo-electrochemical system is shown in Fig. 2-2.

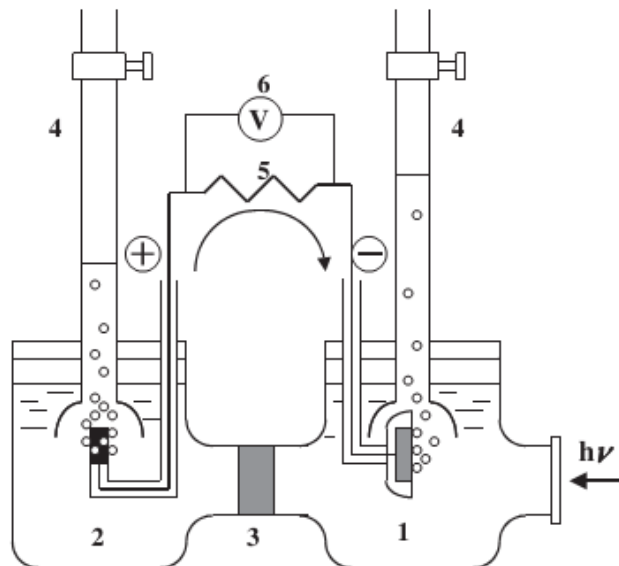
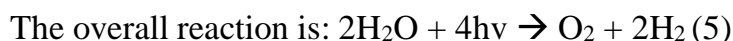
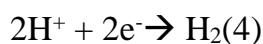
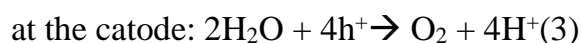
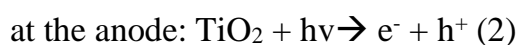


Figure 2-2: Diagram of photo-electrochemical cell. (1): n-type TiO_2 electrode; (2) platinum black counter electrode; (3) ionically conducting separator; (4) gas buret; (5) load resistance; and (6) voltmeter [12]. (Copyright (2005) The Japan Society of Applied Physics)

Under UV irradiation with the energy greater than the band gap energy of TiO_2 electrode, the electric current flowed from the platinum counter electrode to the TiO_2 electrode through the external circuit. The oxidation reaction, which generated oxygen, took place at the TiO_2 electrode and the reduction reaction, which generated hydrogen,

at the Pt electrode. These processes indicates the splitting of water, which can be described as the following scheme:



2.1.1.2. Photocatalytic cleaning effect of TiO₂ loaded materials

The self cleaning effect of TiO₂ was first reported by Honda and Fujishima in 1992 when they worked on a TiO₂ coated ceramic tile photocatalyst. Superhydrophilic property of the surface of TiO₂ allows water to spread completely across the surface rather than remaining as droplets under UV irradiation. Fig. 2-3 shows changes in the contact angle of TiO₂ surface when exposed in dark and under UV light. Honda and Fujishima found that the contact angle of water droplets on the TiO₂ surface start decreasing when this surface is exposed to UV light. The surface becomes superhydrophilic when the contact angle reaches 0°. Longer exposure of TiO₂ surface under UV light results in a drastic decrease of the contact angle. The opposite trend is observed in case of dark exposure condition. The surface retains a low contact angle for a few days under no UV irradiation. The contact angle then slowly increases, which indicates less hydrophilic state of the TiO₂ surface. The surface turns more hydrophilic again when coming into contact with UV light.

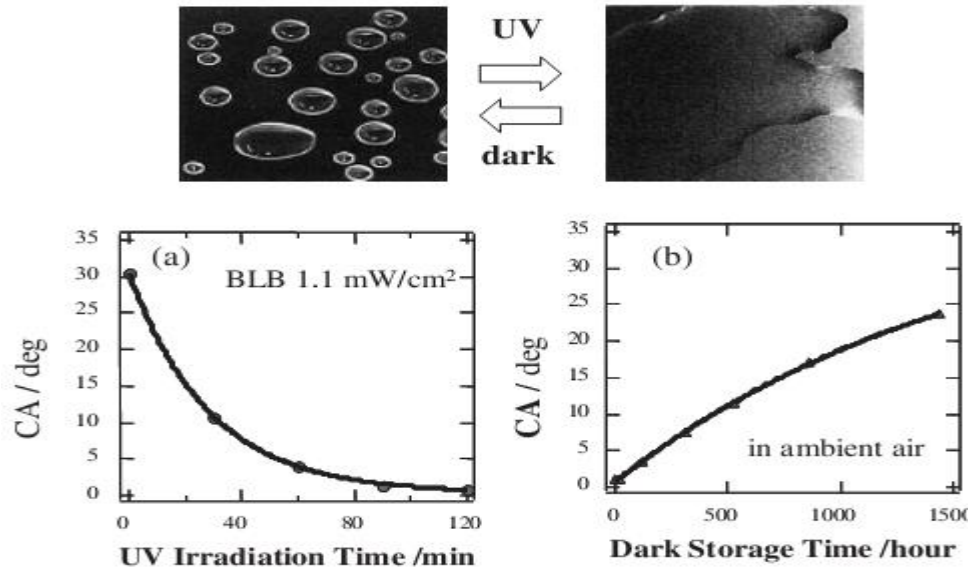


Figure 2-3: Effect of the UV exposure on the contact angle of TiO₂ surface. (a) under UV irradiation, and (b) in dark [12]. (Copyright (2005) The Japan Society of Applied Physics)

According to Honda and Fujishima, this superhydrophilic state is a metastable state, which is driven by photoinduced holes under UV light. Those species transfer from the bulk to the surface of TiO₂ and are trapped at lattice oxygen sites. Most trapped holes then react with the organic compounds or water adsorbed on the surface to produce OH radicals. Some holes may react with TiO₂, breaking the Ti-O bonds by coordinating with water molecules at the surface sites. Such process may release a proton and lead to a formation of a new OH group, which results in the increase of the number of OH groups at the surface (Fig. 2-4). The mono-coordinated OH groups produced by UV light are thermodynamically less stable than the di-coordinated OH groups. Therefore, the surface energy of TiO₂ in the former case is higher than that in the later. The thermodynamically less stable water droplets tend to spread across the TiO₂ surface to become more thermodynamically stable.

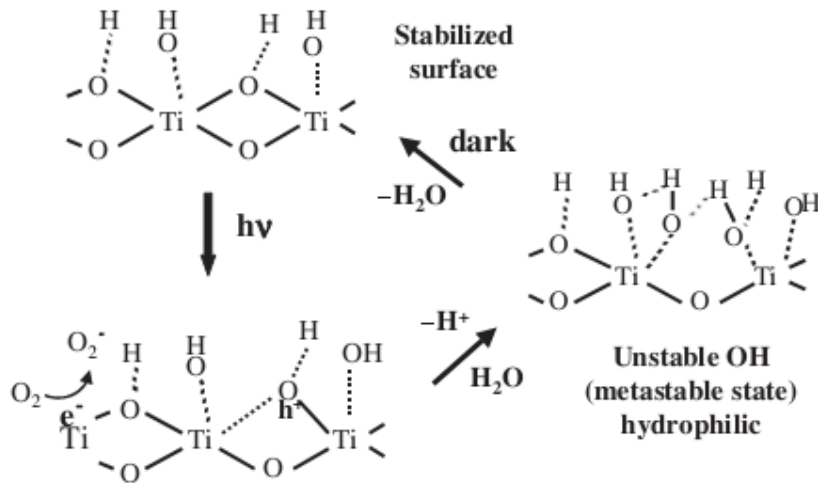


Figure 2-4: The schematic illustration of transformation of the superficial OH groups under UV and in dark [12]. (Copyright (2005) The Japan Society of Applied Physics)

The superhydrophilicity and the intrinsic photocatalytic activity of TiO₂ enhance the self cleaning activity of TiO₂ via the decomposition of adsorbed organic pollutants on TiO₂ surface.

2.1.1.3. Photocatalytic antibacterial effect of TiO₂ loaded materials

In addition to the self- cleaning function of TiO₂, its antibacterial function has been also reported. The strong oxidizing power of TiO₂ is mainly responsible for its antibacterial activity. This function is markedly enhanced under UV light or even visible light with the aid of either silver or copper [17-19]. For example, Fig. 2-5 shows the mechanism of E.coli disinfection for the copper doped TiO₂ material under weak UV light. It is obvious that two steps are involved in the process. Firstly, the reactive photoinduced species attack the outer membrane. The second step is the intercalation of copper ions into the cytoplasmic membrane. These processes are driven by the photocatalytic reaction of TiO₂. Therefore, the E.coli cells are effectively killed on the Cu doped TiO₂ material.

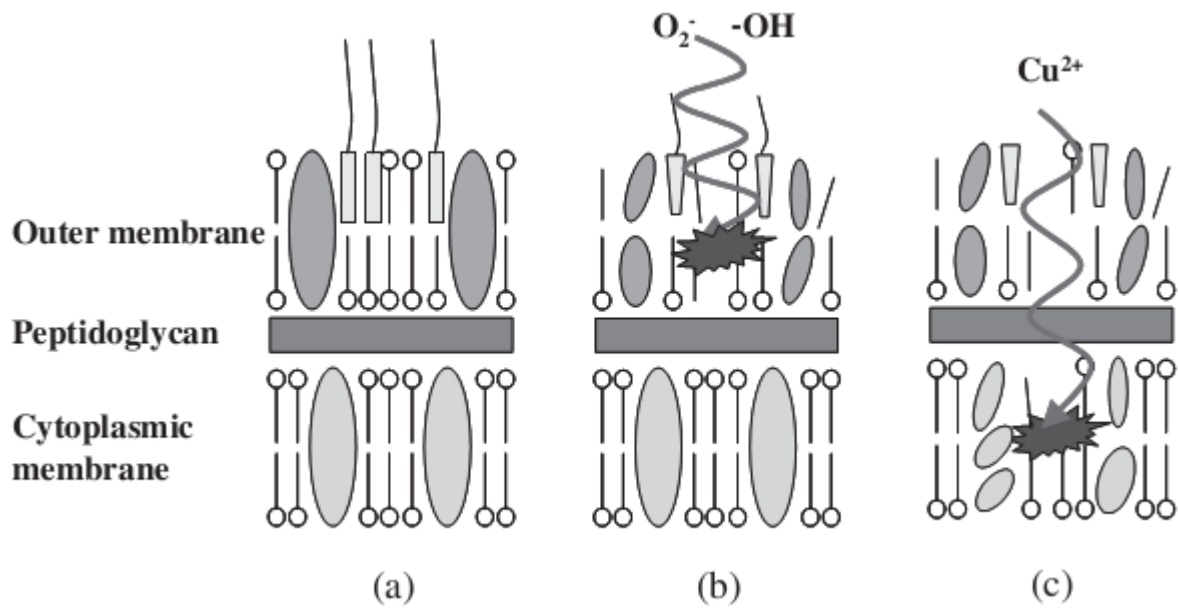


Figure 2-5: Mechanism of E.coli disinfection for the copper doped TiO₂ material under weak UV light [12]. (Copyright (2005) The Japan Society of Applied Physics)

2.1.2. TiO₂ structure and properties

TiO₂ is typically an n-type semiconductor and exists as three different polymorphs: anatase, rutile and brookite (Fig. 2-6). The band gap energy is 3.2 eV for anatase, 3.0 eV for rutile, and 3.2 eV for brookite. Rutile is the primary source and the most stable form. The metastable anatase and brookite will rapidly transform to the thermodynamically stable rutile at calcination temperatures exceeding 600^oC. Titanium atoms exist as six coordinates with six oxygen atoms, forming TiO₆ octahedra, in all three polymorphs.

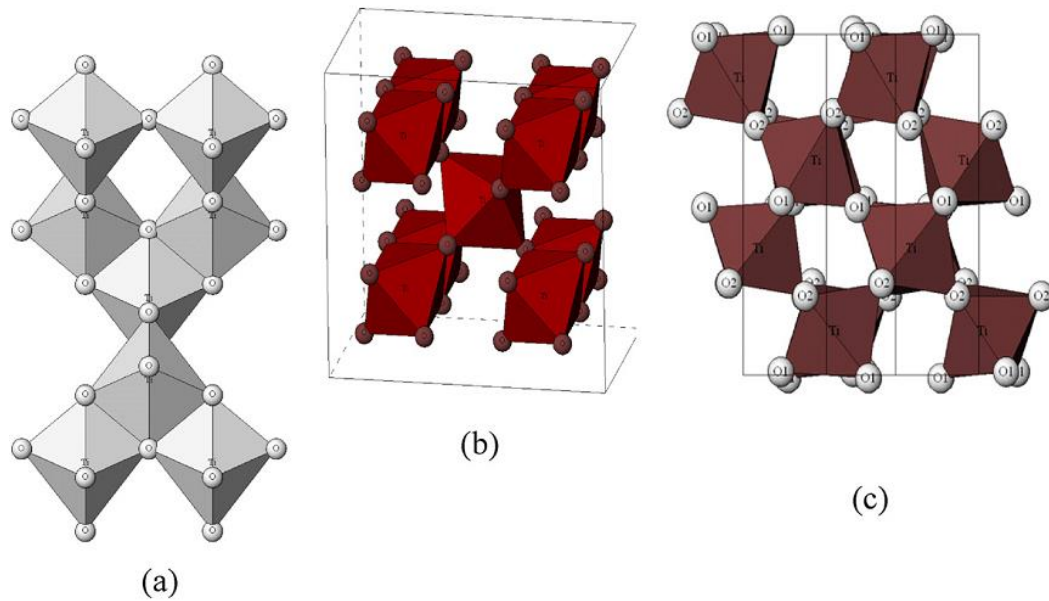
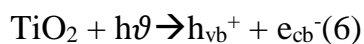


Figure 2-6: Crystalline structures of titanium dioxide (a) anatase, (b) rutile and (c) brookite [13].
(Copyright (2012) Elsevier)

TiO₂ is widely used as a photocatalyst due to its effective photoactivity. Photocatalysis is the process in which a material, usually a semiconductor, absorbs light of sufficient energy to produce reactive species which can lead to an oxidizing degradation of pollutants. Those reactive species are charge carriers such as electrons and holes generated from the photoinduced excitation of TiO₂. Two parallel processes are involved during the photocatalytic reaction. The first is the oxidation of dissociatively adsorbed H₂O by photogenerated holes. The second is the reduction of dissolved oxygen by photoinduced electrons. These processes lead to the release of hydroxyl and superoxide radicals, respectively. In case of TiO₂, when it is irradiated with light of energy greater than its band gap, an excited electron (e_{cb}^-) will be shot out of the valence band to the conduction band, generating a positive hole in the valence band (h_{vb}^+):



Holes and electrons can be trapped as Ti^{3+} and O^- defect sites, respectively. Alternatively, they also can recombine either in bulk or on the surface and emit energy, or transferring to the catalyst surface to react with adsorbed pollutants producing reactive species (Fig. 2-7).

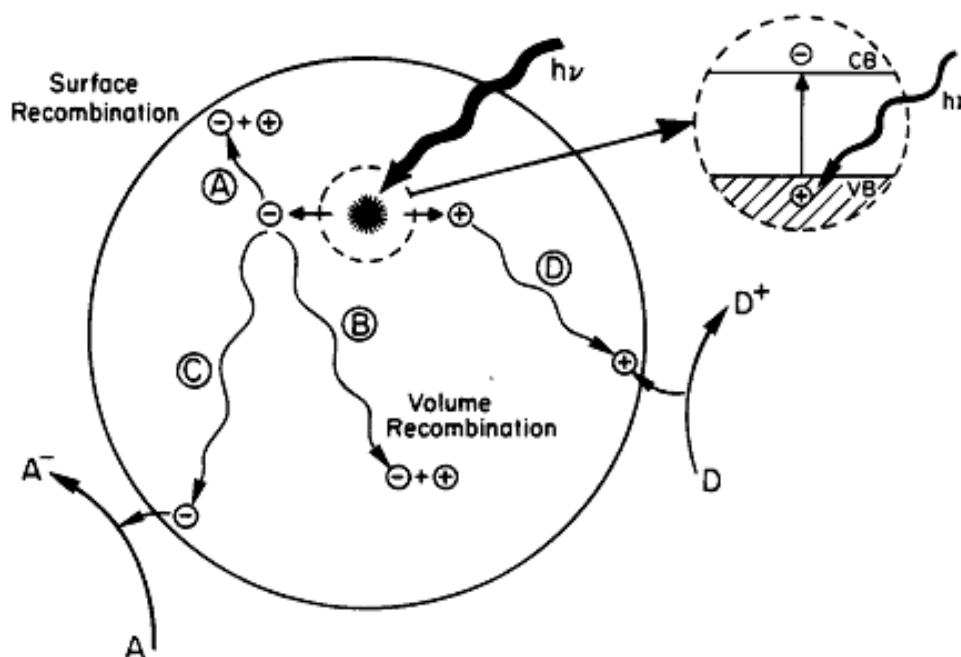
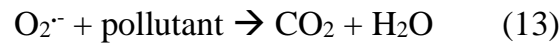
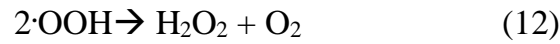
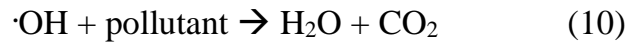
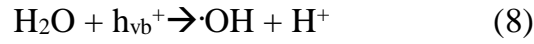


Figure 2-7: Schematic illustration of the photoexcitation and charge-carrier recombination in TiO_2 photocatalyst [14]. (Reprinted with permission from [14]. Copyright (1995) American Chemical Society)

Positive holes can oxidize OH^- or adsorbed water at the surface to produce $\cdot\text{OH}$ radicals. The hydroxyl radicals can subsequently oxidize organic compounds to release mineral salts, CO_2 and H_2O . Electrons in the conduction band are completely trapped by adsorbed oxygen molecules, which leads to the formation of superoxide radical anions (O_2^-). Superoxide radicals may further react with H^+ to generate hydroperoxide radicals

($\cdot\text{OOH}$), which may combine each other to yield H_2O_2 . The following equations are the reactions involved in the whole process.



Photocatalytic activity of TiO_2 depends on its properties such as surface area, charge recombination and interfacial charge transfer dynamics, particle size, crystallinity, density of surface functional groups and defects, etc. in most heterogenous reactions, the surface area and surface functional groups are critical factors. Although it may be controversial that the photodegradation of pollutants take place in bulk of solution or on the surface, higher surface area and more functional groups have been believed to provide more surface adsorption sites on which substrate molecules react with holes. Therefore, the incorporation of functional groups into the TiO_2 template is essential to enhance the adsorption capacity of TiO_2 . Accordingly, the photoactivity of TiO_2 is also improved.

2.2. Strategies for enhance TiO₂ photocatalytic activity

Since TiO₂ has a wide band gap (~ 3.2 eV), its photocatalytic activity is only remarkable under irradiation of UV-light with high photon energy. As it can activate with UV light, TiO₂ can utilize only 3–4% of the solar energy that reaches the earth. The wide band gap of TiO₂ restricts the utilization of visible light which occupies large part of solar light. Moreover, high recombination rate of electrons and holes in TiO₂ results in a low quantum yield and poor photocatalytic activity. Therefore, several methods have been adopted to develop visible-light-driven TiO₂-based photocatalysts, which can be classified as morphological modification and chemical modification.

2.2.1. Morphological modification

In order to enhance the photocatalytic activity of TiO₂, fabrication of solid nanoparticles with well-defined size and high crystallinity has drawn much attention due to their high surface area and more active sites [15]. It has been documented that the photodegradation of adsorbed substrates on TiO₂ nanocatalysts with low particle size and high surface area is more efficient than TiO₂ catalysts with larger diameter and lower surface area [16]. On the other hand, the photodegradation of non-adsorbed substrates is favorable by TiO₂ photocatalysts with large particle size and high crystallinity [17]. Up-to-date, the application of solid TiO₂ nanoparticles, however, is still very limited in wastewater treatment due to the agglomeration of TiO₂ nanoparticles, difficult separation of suspended TiO₂ powder from the treated water, no ability for utilization of visible light, and low mass transfer of pollutants into the surface of TiO₂ for the associated surface mediated reactions [18].

How to enhance adsorption amount of organic pollutants onto the surface of TiO₂ is another method to improve the photocatalytic activity of TiO₂. The introduction of porous structure in TiO₂ has been proved to benefit the mass transfer of pollutants due to large pores in comparison of solid TiO₂ nanoparticles. Two popular approaches to develop porous TiO₂ materials involve soft-template and hard-template-assisted-methods. The former is related to the use of low molecular weight materials such as surfactants, bi- or tri- block copolymers, ionic liquids and vesicles [18]. Although the porous TiO₂ materials can be easily synthesized via this approach, they usually have a poor crystallinity (amorphous or semi-crystalline framework) and low thermal stability. In contrast, the later involves the use of polymer or copolymer, such as silica, colloidal crystals, and polymer beads [18]. Although template-assisted synthetic methods have been widely used for the development of porous materials, the use of those templates trigger some disadvantages such as surface modification, removal of templates and time-consuming synthetic procedures. Therefore people are seeking template-free methods to overcome these intrinsic shortcomings.

In general, morphological modification has been demonstrated to be effective for the improvement of photocatalytic efficiency by increasing the surface area and adsorption capacity of TiO₂ particles. However, this approach suffers from intrinsic limitations such as agglomeration of TiO₂ nanoparticles, difficult separation of TiO₂ suspended particles from the supernatant and UV dependency. Therefore, other promising strategies to construct TiO₂ spheres with high photocatalytic activity is worth of study.

2.2.2. Chemical modification

It is of growing interest in improving sunlight harvesting ability and enhancing the quantum efficiency of TiO₂ photocatalysts. Recently, modifications of TiO₂ by engineering its structural surface, electrical configuration and band-gap have been proposed to increase the photocatalytic activity of TiO₂. The modifications can be classified into: surface modification, metal/non-metal doping and dye sensitization [19].

2.2.2.1. Surface modification

Although TiO₂ nanoparticles have high surface area and more active sites, its photocatalytic activity is relatively low due to rapid aggregation and poor adsorption capacity, especially for non-polar dyes and organic pollutants. Therefore, construction of organic/inorganic modification on TiO₂ surface is getting much more attention. Surface modification of TiO₂ can be conducted by using electron donors and/or acceptors (dopamine, catechol, carboxyl acid, salicylic acid, etc. [19, 20]), insulating oxide coating (Y₂O₃, ZrO₂, MgO and Al₂O₃), formation of intermediate phase (titanates) and deposition of noble metals (Pt, Au) on the TiO₂ surface. These methods can result in effective charge separation, enhanced visible light absorption and improved photocatalyst stability [21, 22].

2.2.2.2. Doping techniques

Due to a wide band gap of TiO₂, the activation of photocatalysis on TiO₂ requires the incident UV light with high energy, which is not abundant in nature. UV light constitutes only 3 % of the solar spectrum. Therefore, in order to fully utilize the solar energy, doping TiO₂ with metal and non-metals by their incorporation into bulk of TiO₂ or dispersion on surface of TiO₂.

2.2.2.2.1. Metal doping

Deposition of noble metals such as Au, Pt, Ag and Pt on TiO₂ photocatalyst is an effective way to achieve high quantum photocatalytic efficiency due to their plasmon resonance produced by the collective oscillations of surface electrons [23]. The metal nanoparticles can act as a mediator for electron storage and transferring photo-generated electrons from TiO₂ surface to an acceptor. Some advantages can be obtained through metal doping such as effective electron-hole separation, enhancement of the visible light absorption and production of hydroxyl radicals through the reaction with hydrogen peroxide. However, some disadvantages have been also documented. For instance, aggregation of metals on the surface of semiconductors at high concentration of decorating metals could lead to a decrease in light absorption and photocatalytic efficiency. Therefore, an appropriate amount of metals is essential for metal doping TiO₂ photocatalysts with enhanced photocatalytic activity.

2.2.2.2.2. Non-metal doping

To overcome the disadvantages of metal doping such as poor thermal stability, photocorrosion and formation of recombination centers, decoration of TiO₂ structure with non-metals such as C, N, F...has been studied so far [23]. The incorporation of non-metals can create a mid-gap state acting as an electron donor or acceptor in the band gap of TiO₂, which introduces lower band gap and shifts the optical absorption of TiO₂ into the visible-light region. Moreover, the electronic conductivity of TiO₂ could be significantly increased as carbon is used as a dopant.

2.2.3. Sensitization of TiO₂

Some conjugated polymers such as polyaniline, polythiophene, polyvinyl alcohol, polypyrrole and their derivatives can be hybridize with TiO₂ for improvement of light absorption and charge transportation due to their narrow and controllable band gap, easy fabrication, high mobility of photo-induced charge carriers, high stability and low cost [24, 25]. Polymer/ TiO₂ hybrid materials exhibit high efficiency in degradation of organic pollutants under UV light and visible light irradiation.

To combine different semiconductors is another approach in order to attain both good charge separation and efficient harvesting ability of sunlight. Quantum dots sized materials such as CdS, PbS, CdSe and PbSe have been propagated for use as sensitizers with TiO₂. Additionally, some organic dyes such as Chrysoidine G, Thionine, Methylene blue, Rhodamine B, etc. have been also sensitized with TiO₂. Three basic processes are involved in the dye sensitizing photocatalysts: first is the physical/ chemical adsorption of dye sensitizers onto the surface of TiO₂; second, the excitation of adsorbed dyes by visible light; and the final is the injection of electrons from the excited dye with high mobility into the conduction band of TiO₂.

2.3. Application

About 5 million tons of TiO₂ are mass-produced annually, accounting for 85% of worldwide use. Most TiO₂ is used as pigment for paints (65%), plastic (20%), paper (10%) and the rest for catalysts, sunscreens, and, very recently, photocatalysts. Recently, due to the development of modified TiO₂ based photocatalysts, which can work effectively under visible light, use of TiO₂ has rapidly increased, particularly in

environment and energy related fields. For environmental applications, conventional TiO_2 has been extensively studied for water treatment and air purification, known as an effective system to treat several hazardous compounds in contaminated water and air. Senthilnatan et al. utilized different TiO_2 photocatalysts for the degradation of lidane, an organochloride pesticide, under visible light [26]. Phenoxyacid herbicides such as mecropop, chloryalid.. were successfully photodegraded when Fe-, N- doped and undoped heterogeneous TiO_2 were employed under visible light [27]. Volatile organic compounds (VOCs) are hazardous pollutants posing adverse effects on human nervous system when they are emitted into the air. A bifunctional as-synthesized photocatalyst called nitrogen-doped and platinum-modified TiO_2 ($\text{Pt/TiO}_{2-x}\text{N}_x$) was proven effective for the degradation of benzene and other VOC compounds under visible light irradiation [28].

Moreover, water disinfection is also another environmental application of TiO_2 . Over the past ten years, disinfection of water using photocatalysts has drawn much attention with research from lab scale to pilot scale. Visible light activated doped TiO_2 has also been studied in a wide range of disinfection applications, including water purification. Yu et al. reported 96.7% reduction in the Gram positive bacterium *Micrococcus lylae* using sulfur doped titanium dioxide [29]. Wu et al. produced titanium dioxide nanoparticles co-doped with N and Ag whose efficiency of photocatalytic inactivation of *E.coli* under visible irradiation [30].

2.4. Mesoporous materials

2.4.1. Definition and classification

Porous materials created by nature or by synthetic design have found great utility in all aspects of human activities. Their pore structure is usually formed in the stages of crystallization or by subsequent treatment and consists of isolated or interconnected pores that may have similar or different shapes and sizes. Porous materials with small pore diameters (0.3 nm to 10 μm) are being studied for their molecular sieving properties. The pore shape can be roughly approximated by any of the following three basic pore models, (a) cylindrical (b) ink-bottled and (c) slit-shaped pores [31, 32].

Depending on the predominant pore sizes, the porous solid materials are classified by IUPAC: Microporous materials, (1), having pore diameters up to 2.0 nm; mesoporous materials, (2), having pore sizes intermediate between 2.0 and 50.0 nm; and macroporous materials, (3), having pore sizes exceeding 50.0 nm.

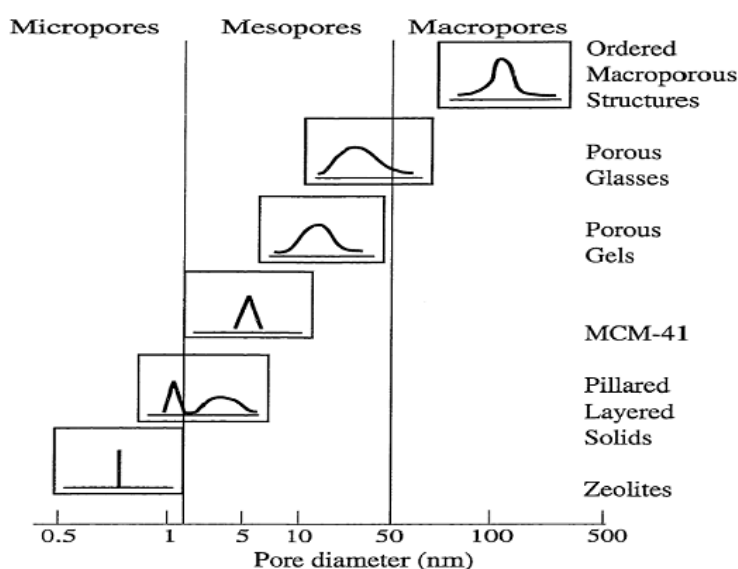


Figure 2-8: Classification of porous materials in respect to pore size [33]. (Reprinted with permission from [33]. Copyright (1996) American Chemical Society)

Porosity of a material is usually defined as the ratio of the volume of pores and voids to the volume occupied by the solid. The term adsorption originally denoted the condensation of gas on a free surface. Adsorption of a gas by a porous material is described quantitatively by an adsorption isotherm, the amount of gas adsorbed by the material at a fixed temperature as a function of pressure. Porous materials are most frequently characterized in terms of pore sizes derived from gas sorption data, and IUPAC conventions have been proposed for classifying pore sizes and gas sorption isotherms that reflect the relationship between porosity and sorption. The IUPAC classification of adsorption - desorption isotherms is illustrated in Fig. 2-9. The six types of isotherm (IUPAC classification) are characteristic of adsorbents that are microporous (type I), nonporous or macroporous (types II, III, and VI), or mesoporous (types IV and V).

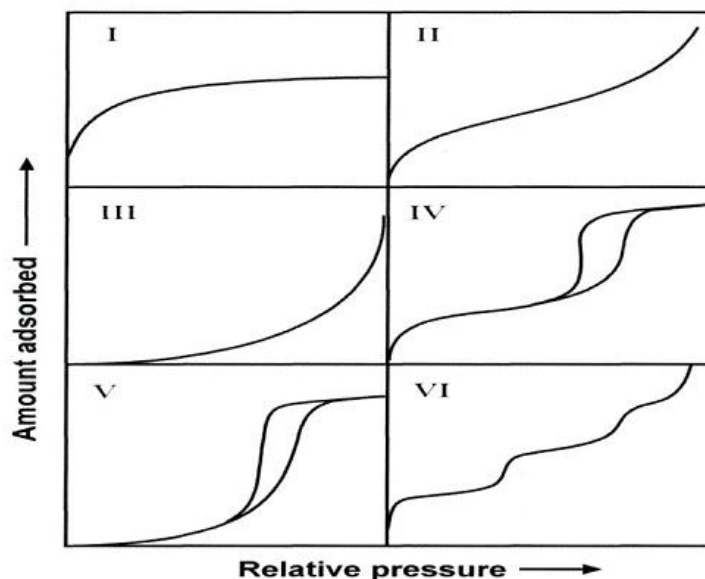


Figure 2-9: The IUPAC classification of adsorption - desorption isotherms [34]. (Copyright (1976) American Institute of Chemical Engineers)

2.4.2. Application of mesoporous materials

Contamination of water streams by transition metals, heavy metals, and radioactive compounds (e.g., nickel, copper, lead, mercury, cadmium, uranium, and thorium) remains a concern in the field of environmental remediation. These materials enter the environment through a variety of avenues that include: mining, nuclear power plants, and industrial processing plants. Furthermore, some natural waters contain naturally high concentration levels of metals [34]. The presence of even low concentrations (ppb) of some heavy metals or radioactive substrates in natural water systems can have a harmful effect on both wildlife and humans. However, at these low concentrations of metal ions the sample often requires pre-concentration before analysis can be undertaken. Adsorption onto solid substrates (e.g., activated carbons, zeolites, aluminas, and silicas) provides one of the most effective means for adsorption, separation and removal of trace pollutants (heavy metal ions, radioactive compounds, etc.) from aqueous streams. A wide variety of novel materials can be prepared by the chemical modification of mesoporous materials, since numerous organic and inorganic functionalities can be used for this purpose. In addition to their use in chromatographic separations, these materials have been increasingly used as heterogeneous catalysts in liquid phase organic reactions. It is their characteristics, such as viability and environmental safety, which makes them alternatives to traditional absorbent materials such as activated charcoal and zeolites. Their use as efficient materials for the selective adsorption and separation, and high capacity uptake of trace metals from aqueous systems is due to their unique characteristics such as high surface area, large pore size, and presence of reactive groups on the surfaces [35].

2.5. Sol-gel method

2.5.1. Overview

Organic/ inorganic hybrid materials prepared by the sol-gel approach have rapidly become a fascinating new field of research in materials science. The explosion of activity in this area in the past two decades has resulted in tremendous progress in both the fundamental understanding of the sol-gel process and the development and applications of new organic/inorganic hybrid materials. Sol-gel chemistry has been investigated extensively since the 1970's, when sol-gel reactions were shown to produce a variety of inorganic networks. Sol-gel reactions are those which convert an aqueous metal alkoxide $[M(OR)_n]$ solution into an inorganic network. It is a wet chemical route to synthesis of a colloidal suspension of solid particles or clusters in a liquid and subsequently to formation of a dual phase material of a solid skeleton filled with a solvent through sol-gel transition. A sol is defined as a solution of suspended colloidal solid particles. A gel, on the other hand, is a solid network filled with a second phase of colloidal dimensions, either liquid or gas that also forms a three dimensional inter-connected network. In the sol preparation, the precursors which are metals or metalloids bound to various reactive ligands undergo two chemical processes: hydrolysis and condensation or polymerization, typically with acid or base as catalysts, to form small solid particles or clusters in a liquid. Metal alkoxides are the reagents most used due to their ease of hydrolysis in the presence of water. Fig.2-10 represents the sol-gel reaction of tetraethoxysilane (TEOS) precursors as an example.

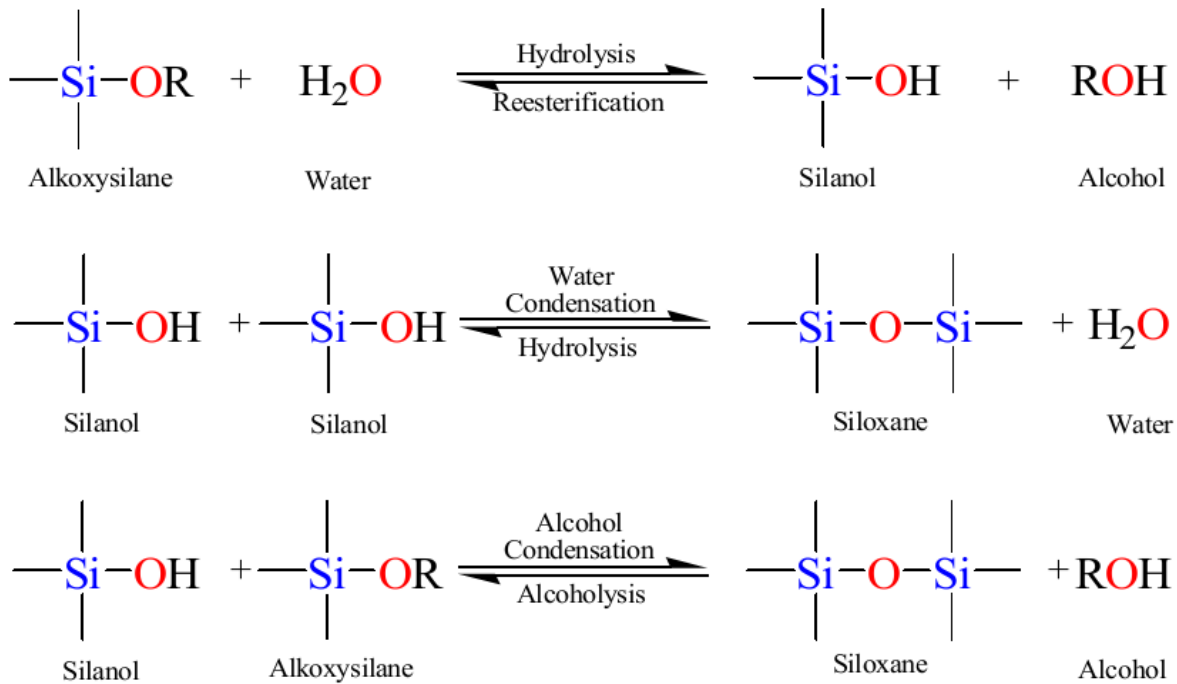


Figure 2-10: Scheme of sol-gel reaction [35].

2.5.2. Contributing factors in sol-gel process

2.5.2.1. Water-to-alkoxide Ratio

The silica content of the formed gel increases upon increasing the water-to-alkoxide ratio. The water condensation step was found to be accelerated upon increasing the water-to-alkoxide due to the increase in the solubility of silica and the increase in the concentration of hydroxyl ion catalyst. Moreover, alcohol condensation was promoted at the water/alkoxide ratio less or equal to 2, while water condensation was promoted at higher ratios. The water-to-alkoxide ratio also influences the structure of the obtained gel network. It is the result of the completion of hydrolysis and the occurrence of auxiliary condensation with the presence of a abundant amount of water.

2.5.2.2. Characteristics and dose of catalysts

The rates and mechanisms of hydrolysis and condensation reactions are strongly affected by the identity of the catalyst. In acid catalysis (Fig. 2-11), the first step in hydrolysis is electrophilic attack of the proton on an alkoxy oxygen atom, leading to the development of a positive charge on it. This electrophilic attack also makes the bond between the silicon center and the attacked oxygen (Si–O) more polarized and facilitates its breakage in the departure of the alcohol leaving group. The rate-controlling step in acid hydrolysis is an S_N2 nucleophilic attack of water oxygen on the silicon from the backside. It was also found that the hydrolysis reaction was first-order with respect to water concentration under acidic conditions. Accordingly, an increase in the water to alkoxy ratio resulted in an increase in the rate of hydrolysis. However, the enthalpy of the hydrolysis declined upon increasing extent of hydrolysis.

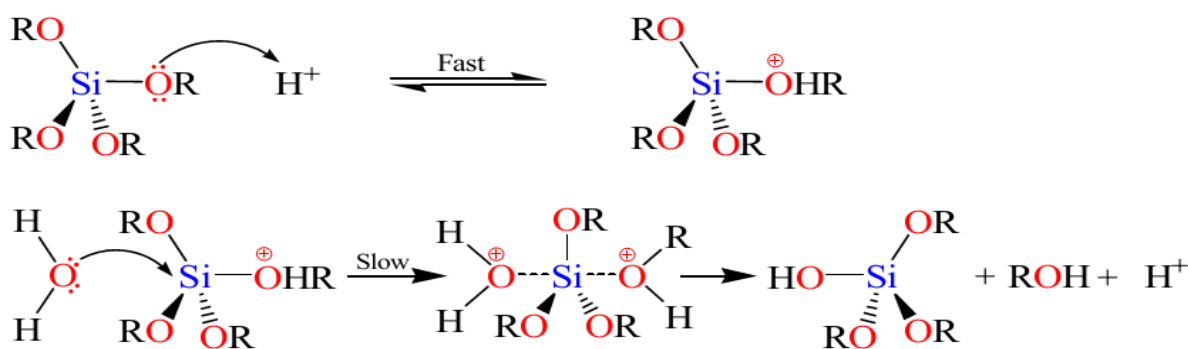


Figure 2-11: Hydrolysis mechanism of an alkoxy silane using acidic catalyst [35].

The condensation rate and mechanism were found to depend on the pH of the reaction. For instance the condensation reactions become irreversible at low pH because the solubility of silica and its rate of dissolution are insignificant. The mechanism of condensation under acidic conditions is depicted in Fig. 2-12. The first step is the fast

step and is an electrophilic attack of the proton on the oxygen of the silanol group. This attack results in the silanol oxygen becoming positively charged. The second step is the formation of a siloxane bridge via the loss of a hydronium cation (the catalyst) as a result of the condensation between a protonated silanol groups with an unprotonated one. Noticeably, the first steps in both hydrolysis and condensation reactions are similar.



Figure 2-12: Condensation mechanism of an alkoxy silane using acidic catalyst [35].

When a base catalyst is used for the formation of silica, the hydroxide ion serves as a nucleophile that attacks the silicon atom center of the tetraalkoxy silane in an SN2 hydrolysis step. The result of this step is a silanol and an alkoxide ion. Abstraction of the silanol proton by the hydroxide ion is the first step in the condensation process, leading to the formation of siloxide ion and water. A siloxane linkage is then formed through the SN2 attack of the latter ion on the silicon center of silanol. This step regenerates the hydroxide ion catalyst and is the rate-determining step of the condensation reactions. The hydrolysis and condensation reactions mechanisms are shown below in Fig. 2-13.

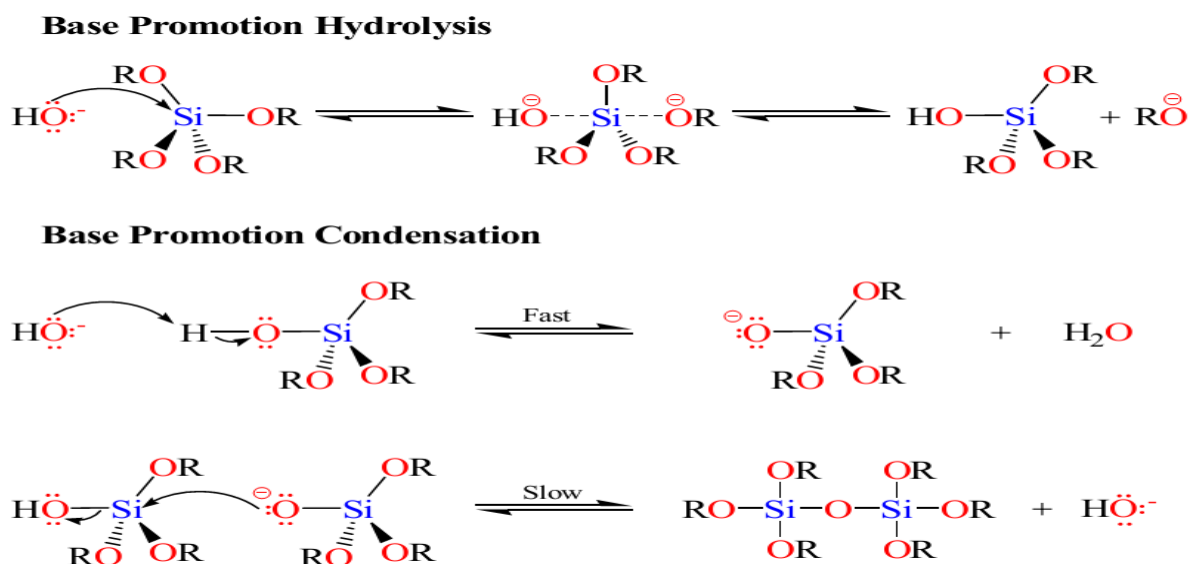


Figure 2-13: Mechanism of an alkoxy silane using basic catalyst [35].

When an acid catalyst is employed, the rate-controlling step is the particle nucleation and the fast step is the hydrolysis. This fact leads to the production of more linear-like networks with less siloxane bonds and a high concentration of silanol groups, and hence, minimally branched polymeric species. On the other hand, alkoxy hydrolysis by base catalyst is faster than acid and prevents the quick aggregation of sol particles resulting in highly dense materials with fewer silanol groups in the overall network.

2.5.3. Advantages and drawbacks of the sol-gel method

Advantages

- * Undertake high purity of synthesized materials.
- * Synthesize materials with high homogeneity.
- * Low processing temperature.
- * Environmentally friendly.

Disadvantages

- * High cost.
- * Large shrinkage during processing.
- * Residual fine pores and hydroxyls.
- * Easily cracking during the drying stage.
- * Time consuming

2.6. Dyes and treatment methods

2.6.1. Classification of dyes

Dyes can be classified in terms of chemical structure, colour and applications. The classification of common dyes based on their chemical structures is presented in Table 1. On the other hand, Table 2 shows the different applications of dyes used to characterize each dyes. Due to the complexity of the chemical structure and colour of dyes, the classification based on their applications is often favorable. Another way of classification is based on their particle charge in aqueous solution such as cationic (all basic dyes), anionic (direct, acid, and reactive dyes), and non-ionic (dispersed dyes).

Table 1: Classification of dyes in term of chemical structure [36].

Class	Chromospheres	Example
Azo dyes		 Reactive Black 5
Anthraquinone dyes		 Reactive Blue 4
Indigoid dyes		 Acid Blue 71
Nitroso dyes		 Acid green 1
Nitro dyes		 Acid Yellow 24
Triarylmethane dyes		 Basic Red 9

Table 2: Classification of dyes according to method of application [37].

Class	Substrate	Application	Types of dye
Acid	Wool, nylon, silk, inks, leather, paper.	from neutral to acidic bath	Anthraquinone, xanthene, azo, nitro, and triphenylmethane.
Basic	Inks, paper, polyacrylonitrile, treated nylon, and polyester	acidic dye baths	Hemicyaninemazom cyanine, diazahemicyanine, azine, anthraquinone and oxazine
Direct	Nylon, rayon, paper, leather and cotton	neutral or a little alkaline bath containing additional electrolyte.	Phthalocyanine, azo, oxazine, and stilbene.
Disperse	Polyamide, acrylic polyester, acetate, and plastics	High temperature/pressure or lower temperature carrier methods, dye may be padded on cloth and thermo fixed	Benzodifuranone, azo, anthraquinone, nitro, and styryl.
Reactive	Wool, cotton, silk and nylon	Reactive site on dye reacts with functional group on fibre to bind dye covalently under influence of heat and pH	Anthraquinone, formazan, phthalocyanine, azo, oxazine and basic
Sulfur	Rayon and cotton	Aromatic substrate treated with sodium sulphide and reoxidized to insoluble sulphur-containing products on fibres	Indeterminate structures

2.6.2. Toxicity of dyes

A small portion of basic dyes in wastewater can cause high intensity of colours. Dyes have been found to affect the photosynthetic activity of aquatic life by preventing the penetration of sunlight into aqueous environment, and may also be toxic to some aquatic species due to the presence of metals, aromatics, etc. Moreover, dyes have been believed to trigger carcinogen, mutagen, or teratogen for not only living organisms but human beings also. Additionally, they can lead to severe damage to human beings' organs such as malfunction of the kidney, reproductive system, liver and nervous system. The toxicity of azo dyes is due to the presence of amines in the effluent. Anthraquinone based dyes are low biodegradability, which is harmful to aquatic life. Also, dyes are soluble in water, causing serious problems to the environment. Due to their toxicity, methods to remove them from effluents have drawn much concern.

2.6.3. Dye treatment methods

There are various methods to treat dye loaded effluents. The technologies can be divided into three groups: physical, chemical and biological methods. Each of them has their own advantages and disadvantages. Table 3 shows the advantages and disadvantages of different dye removal methods [38].

Table 3: Advantages and disadvantages of different dye removal methods.

Categories	Methods	Advantages	Disadvantages
	Adsorption by activated carbon	Good removal of wide variety of dyes	Very expensive

Physical treatment	Membrane filtration	Removes all dye types	Concentrate sludge
	Ion exchange	Regeneration: no adsorbent loss	Not effective for all dyes
	Irradiation	Effective oxidation at lab scale	Requires a lot of dissolve O ₂
Chemical treatment	Oxidative process	Simplicity	Agent needs to be activated
	Fenton's process	suitable chemical method	Sludge generation
	Ozonation	Ozone can be applied in its gaseous state and does not increase the volume of waste water and sludge	Short half life
	Photochemical	No sludge is produced and foul odours are greatly reduced	Formation of by-products
	Sodium hypochlorite (NaOCl)	Initiates and accelerates azo-bond cleavage	Release of acromatic amines

	Electrochemical destruction	No consumption of chemicals and no sludge buildup	Relatively high flow rates cause a direct decrease in dye removal
Biological treatment	Decolourization by white-rot fungi	White-rot fungi are able to degrade dyes using enzymes	Enzyme production has also been shown to be unreliable
	Other microbial culture	Decolorised in 24-30 h	Under aerobic conditions azo dyes are not readily metabolised
	Adsorption by living/dead microbial biomass	Certain dyes have a particular affinity for binding with microbial species	Not effective for all dyes

CHAPTER 3. EDTA-NA₂-ASSISTED SYNTHESIS OF ROD-LIKE TITANATE-TIO₂ COMPOSITE ARCHITECTURES

In this chapter, we report a simple fabrication of visible-light-driven titanate-TiO₂ rod-like composites through a EDTA-NA₂-assisted route. The adsorption ability and photocatalytic activity of the as-synthesized samples at different amounts of EDTA-NA₂ were tested via the degradation of methylene blue (MB) in dark and under visible light. Moreover, mechanisms for the formation of titanate-TiO₂ rod-like heterojunctions, and for the MB removal were also investigated in detail.

3.1. Preparation of the composite

3.1.1. Chemicals

EDTA-NA₂ (≥ 99.0 %), acetic acid (≥ 99.7 %), titanium (IV) isopropoxide (TTIP, ≥ 99.99 %), isopropanol (ISP, ≥ 99.7 %), tert-butanol (t-BuOH, ≥ 99.0 %), p-benzoquinone (BQ, ≥ 98 %) and MB (≥ 95.0 %) were purchased from Sigma-Aldrich and were used for experiments without further purification. Deionized (DI) water from a Millipore water (18 MΩ.cm) purification system was used for all experiments.

3.1.2. Preparation of photocatalysts.

A 50.0 mL mixture (1:2, v/v) of TTIP and ISP was added drop-wisely to 100 mL of a solution containing different amounts of EDTA-Na₂ and 1.40 mL of acetic acid under vigorous stirring at 4 °C for 3 h. The obtained solutions with different ratios of EDTA-Na₂ and TTIP (defined as xEDTA-Na₂/TiO₂ where x = 0.5, 1.0, 1.5 at %) were placed in the dark for aging in 24 h. Solvent evaporation was performed in vacuum at 80 °C for 1 h with the aid of a rotary evaporator, followed by drying in an oven at 105 °C. The dried samples were then calcined in air at 400 °C for 3 h. For comparison, the pristine TiO₂ was synthesized using the same process but in the absence of EDTA-Na₂. All reagent-grade chemicals were used without pretreatment.

3.1.3. Characterization.

The morphology of the as-synthesized materials was determined by using field emission - scanning electron microscopy (FE-SEM, SU 8220, operated at 10 kV with Pt sputter coating) coupling with energy – dispersive X-ray (EDX) spectroscopy. The specific Brunauer-Emmett-Teller (BET) surface area and pore size measurements of the samples were investigated on a Micromeritics ASAP 2020 apparatus under nitrogen atmosphere. The pore size distribution was calculated from Barrett-Joyner-Halenda (BJH) desorption branches of isotherms. The crystal phases of the as-synthesized samples were analyzed by X-ray diffraction (XRD) patterns using a Bruker D8 advance powder diffractometer model (Copper anode, working condition: 40kV/ 30mA, scanning type: continuous scanning, 2θ = 10 – 70°). The Raman spectra of samples were recorded on a LabRam HR micro-Raman instrument with a 532 nm Ar⁺ ion laser at a room temperature. The chemical composition of the samples was analyzed based on X-

ray photoelectron spectroscopy (XPS) data recorded on a Thermo Scientific Sigma Probe spectrometer with a monochromatic AlK α source (photon energy 1486.6 eV), spot size 400 μ m, pass energy of 200 eV and energy step size of 1.0 eV. For high resolution XPS spectra of elemental components, pass energy of 50 eV and energy step size of 0.10 eV were used. Triplicate XPS scannings were performed with an accuracy \pm 0.2 eV. For all samples, the C1s peak level was taken as an internal reference at 284.6 eV. All reported binding energy data were taken from high resolution XPS spectra. XPS peaks were deconvoluted by using symmetric Gaussian (Lorentzian) fitting curves. To verify the working optical range of the samples, the UV-vis diffused reflectance spectroscopy (DRS) results of the samples were recorded on a Perkin-Elmer Lambda UV-vis-NIR spectrophotometer, using BaSO₄ as the reference material. Photoluminescence (PL) spectra were collected at room temperature on a PTI luminescence spectrometer with a solid accessory. A Genesis 10S UV-Vis spectrophotometer was used to obtain the absorbance of the MB solution at 665 nm. By-products formed due to the photo-degradation of MB were analyzed with a HPLC-MS with an API 2000 mass spectrometer using an electrospray ionization (ESI) source in a positive mode.

3.2. Photocatalytic activity test

MB (at neutral pH) was used as a testing dye to evaluate the photocatalytic activity of the catalysts. Prior to irradiation with visible light, 20 mg of the synthesized photocatalysts was dispersed into 20 mL of 10 mg/L MB solution placed in a 100 mL quartz photo-reactor equipped with a circulating water system (Fig. 3-1) [39]. The

mixture was placed in the dark condition under vigorous stirring for 30 mins to obtain adsorption-desorption equilibrium. The reactor was then irradiated with a fluorescent lamp (Philips, 14 W, 1 mW/ cm², emission range of 400 – 800 nm, ~ 10 cm above the MB solution) for 2 h. During irradiation, aliquots of MB were taken out at specific time intervals, and centrifuged at 3,000 rpm for 5 mins to remove any solids. The remaining MB concentration was determined using a UV-Vis spectrophotometer. All experiments were triplicated at room temperature. For quality assurance and quality control of the measurements, a blank sample (only MB, without catalysts) was subject to the same procedure under identical conditions.

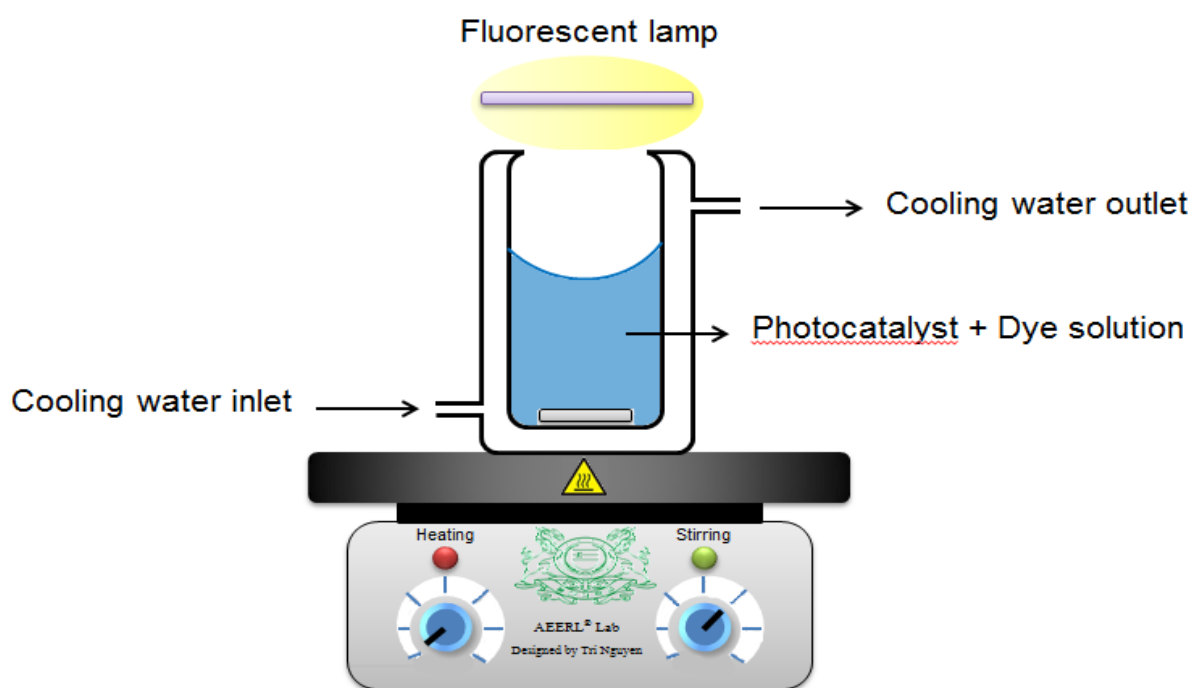


Figure 3-1. Schematic diagram of the photocatalytic reactor.

3.3. Results and discussion

3.3.1. Material properties

3.3.1.1. Structural analysis

Fig. 3-2 (a) shows the XRD patterns of the modified and pristine TiO_2 samples. Whereas the pristine TiO_2 only contains the anatase phase (JCPDS No. 21-1272), the modified samples contain a mixture of anatase and layered titanate $\text{Na}_2\text{Ti}_3\text{O}_7$ (JCPDS No. 31-1329) with a monoclinic lattice (P21/m).[40] The calcined EDTA- Na_2 samples showed a decrease in anatase peak intensity, indicating their poor crystallinity.[41] The deterioration in crystallinity of the modified samples was favored by an increase in EDTA- Na_2 content. The XRD spectra reveal an amorphous structure when the EDTA- Na_2/TiO_2 ratio reached 1.5.

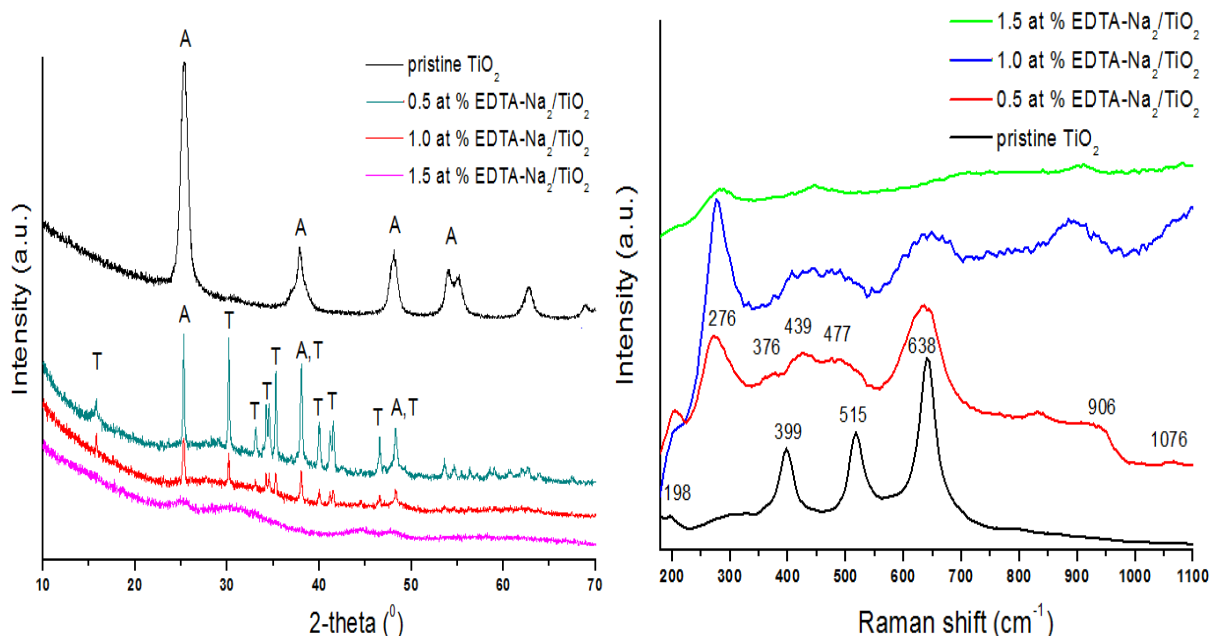


Figure 3-2. (a) XRD and (b) Raman spectra of x at % EDTA- Na_2/TiO_2 and pristine TiO_2 . (A: anatase; T: titanate)

Raman spectroscopy was further used to confirm the phase composition and surface homogeneity of the samples, as shown in Fig. 3-2 (b). Four Raman scattering peaks of the pristine TiO₂ at 198 (E_g), 399 (B_{1g}), 515 (A_{1g} + B_{1g}) and 638 (E_g) cm⁻¹ are those of the anatase phase, which is consistent with the XRD observations. These peaks are weakened, broadened and obscured for all modified samples due to either or both of the following two reasons: first, the heterogeneity of surface activates the zone-edge or Raman forbidden-modes by relaxing the phonon selection rules; and/or second, the intrinsic defects in edge-shared TiO₆ octahedral structure cause phonon scattering and decrease in their lifetime, leading to band broadening [42, 43]. Moreover, other peaks at 276, 376, 439, 477 and 906 cm⁻¹, which are indicative of Na₂Ti₃O₇ [44, 45], were also observed in the Raman spectra of 0.5 at % EDTA-Na₂/TiO₂. The bands at 276 and 439 cm⁻¹ are associated with Na-O-Ti bonds and the framework Ti-O-Ti vibrations, respectively. A shoulder at 906 cm⁻¹ is assigned to the short Ti-O symmetric stretching vibrations related to non-bridging oxygen atoms coordinated with sodium ions. A weak peak at 1076 cm⁻¹ is assigned to carbonaceous species [45]. A high EDTA-Na₂ content causes many defects in the edge-shared TiO₆ octahedral structure and high surface heterogeneity of the modified samples. Obviously, the Raman spectra serve as a further proof of the co-existence of titanate and anatase in the modified samples. The formation of a titanate-anatase hybrid is possible due to the common structural features of the TiO₆ octahedral structure in anatase and titanates [46].

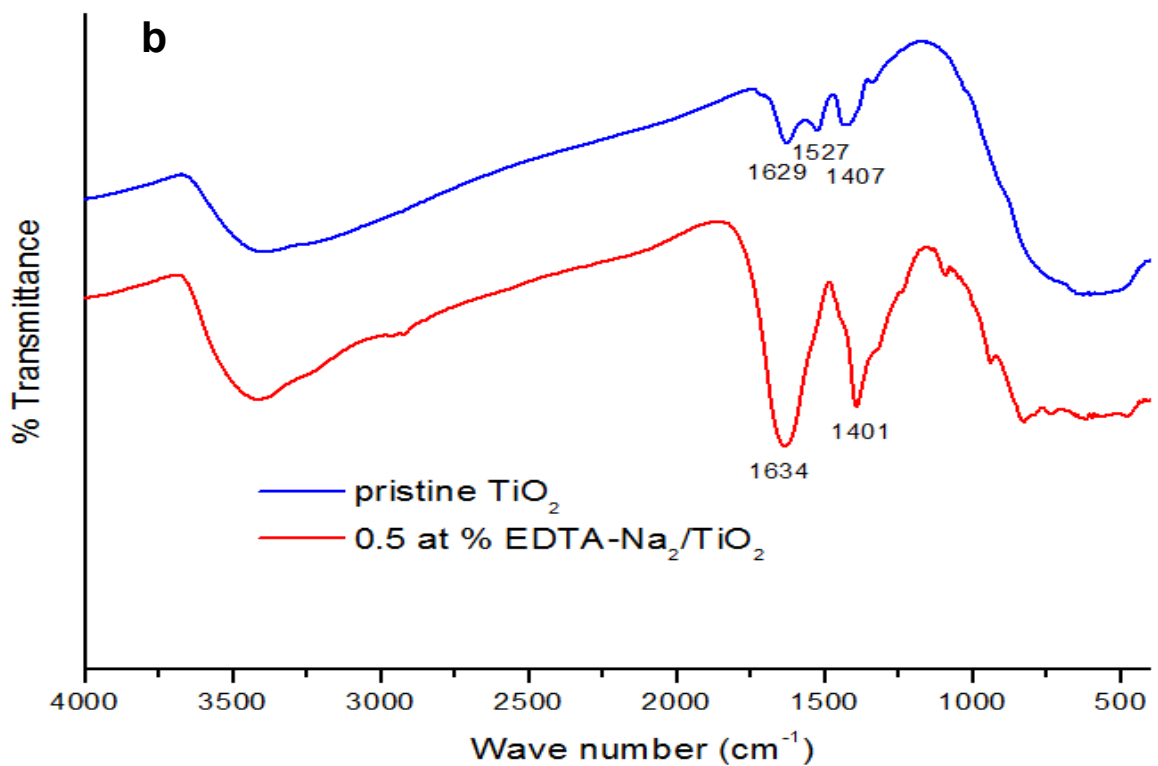
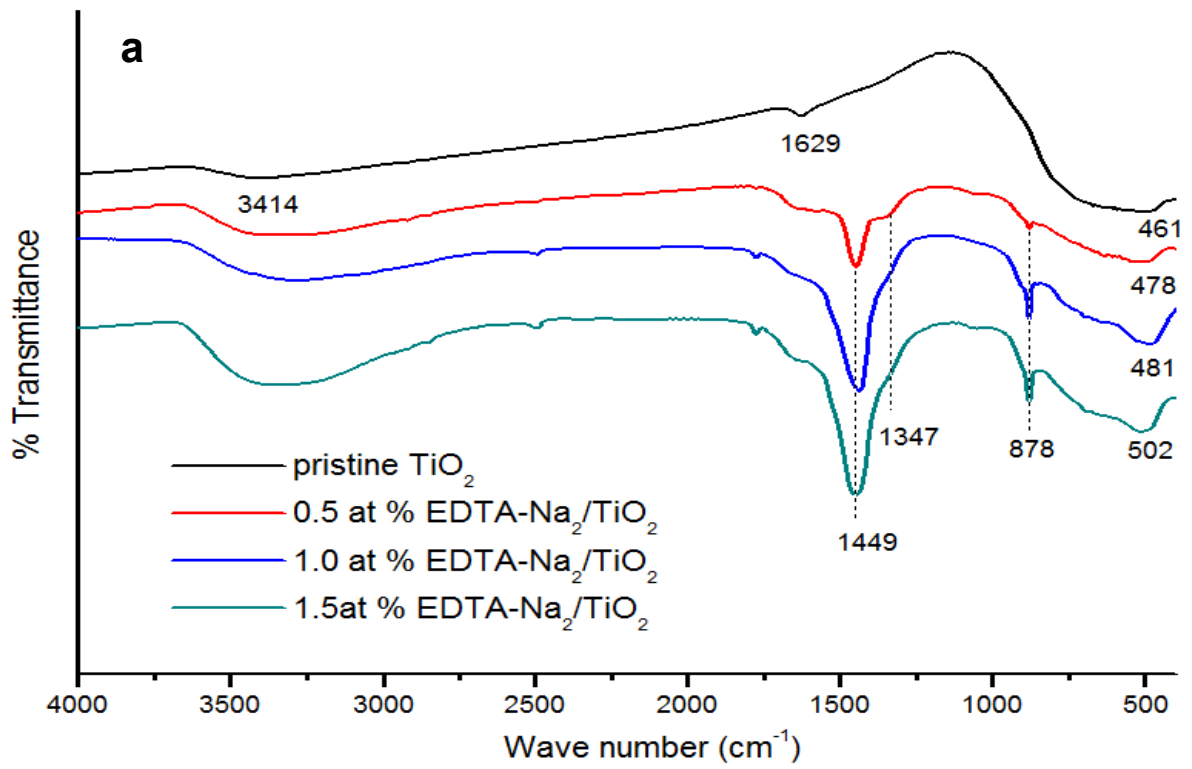
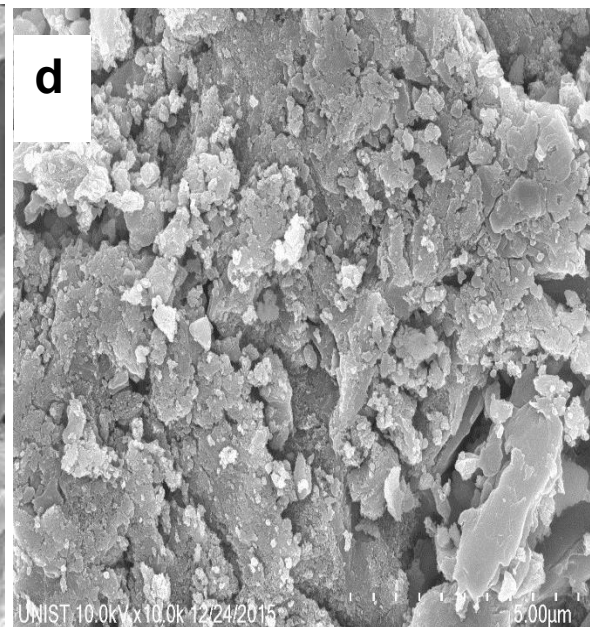
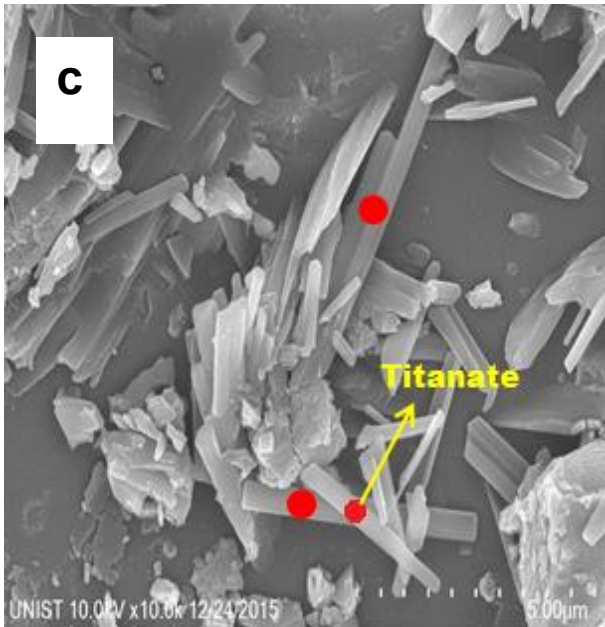
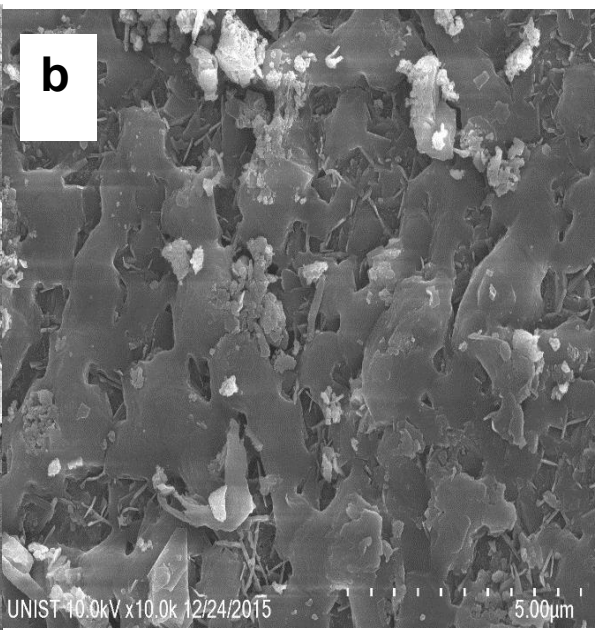
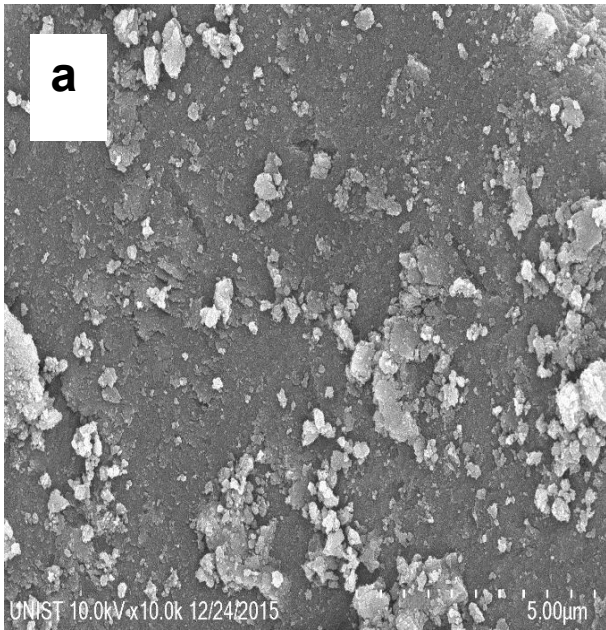


Figure 3-3. a) FTIR spectra of pristine TiO₂ and x at % EDTA-Na₂/TiO₂ (x = 0.5, 1.0, 1.5) obtained at 400 °C. b) FTIR spectra of xerogel pristine TiO₂ and xerogel 0.5 at % EDTA-Na₂/TiO₂

The characteristics of chemical bondings in the samples obtained at 400 °C were also identified by the analysis of FTIR spectra (Fig. 3-3). The pristine TiO₂ exhibited the stretching and deforming vibrations of adsorbed water molecules at 3414 and 1629 cm⁻¹, respectively. It can also be found that a broad peak at 461 cm⁻¹ was detected for the pristine TiO₂, which was attributed to Ti-O-Ti stretching bondings of the TiO₆ octahedral structure. Slightly red shifts of Ti-O-Ti stretching peak ($\delta\nu = 17 - 41$ cm⁻¹) were observed for the modified samples, indicating lattice incorporation of nitrogen dopants [47]. An intensive peak was also observed at 1449 cm⁻¹ for all modified samples, which corresponds to the vibration of polydentate carbonate species[48]. The shoulder at 1347 cm⁻¹ is characteristics of the surface bidentate carbonate species [48], which facilitate the MB adsorption via electrostatic interaction between the cationic MB molecules and the highly electronegative O atoms of carbonate species. Another peak at 878 cm⁻¹ represents the bending vibration of Na-O-Ti bonds of sodium titanate [49]. The intensity of this peak gradually increases with increasing concentration of EDTA-Na₂, indicating effective intercalation of Na⁺ ions into the titanate interlayers.

3.3.1.2. Morphology

Fig. 3-4 (a-d) shows the morphology of the pristine TiO₂ and EDTA-Na₂-modified TiO₂ samples. The surface of pristine TiO₂ was loaded with clusters of nano- to micro-sized particles due to agglomeration of ultrafine TiO₂ powders into larger particles [50]. As compared to the surface of the pristine TiO₂, that of 0.5 and 1.0 at % EDTA-Na₂/TiO₂ shows the presence of irregular rod-like nanostructures to some extent. Those



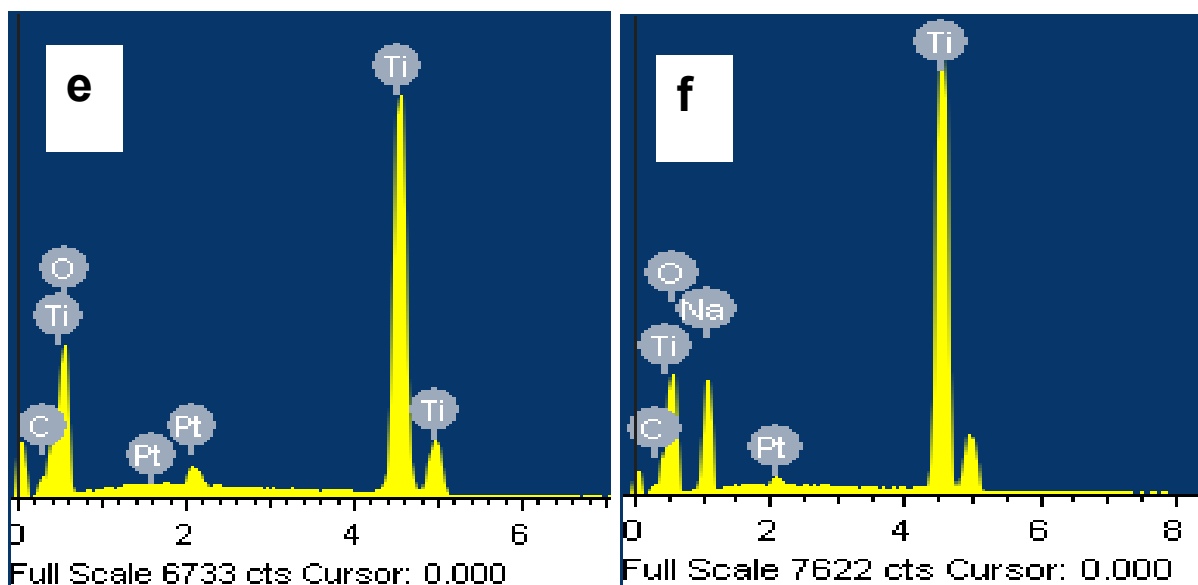


Figure 3-4. FE-SEM of the pristine TiO_2 (a) and 0.5, 1.0, 1.5 at % $\text{EDTA-Na}_2/\text{TiO}_2$ (b, c, d), respectively. EDX of the pristine TiO_2 (e) and 1.0 at % $\text{EDTA-Na}_2/\text{TiO}_2$ (f).

rod-like structures mostly vanished from the SEM image of 1.5 at % $\text{EDTA-Na}_2/\text{TiO}_2$, indicating that the formation of rod-like nanostructures was not favorable at high content of EDTA-Na_2 . Instead, an amorphous morphology was observed for 1.5 at % $\text{EDTA-Na}_2/\text{TiO}_2$. EDX analysis of the pristine TiO_2 (Fig. 3-4e) further confirms that Ti and O are the most dominant elements, whereas that of 1.0 at % $\text{EDTA-Na}_2/\text{TiO}_2$ (Fig. 3-4f) reveals the presence of sodium (Na) in comparison with its absence in the pristine sample. The Ti/Na ratio (at %) was estimated as 1.6, suggesting the formation of sodium tri-titanate ($\text{Na}_2\text{Ti}_3\text{O}_7$) [44, 51]. Moreover, the SEM mapping images of 1.0 at % $\text{EDTA-Na}_2/\text{TiO}_2$ (Fig. 3-5) further confirm the heterogenous distribution of sodium tri-titanate nanorods on the TiO_2 surface.

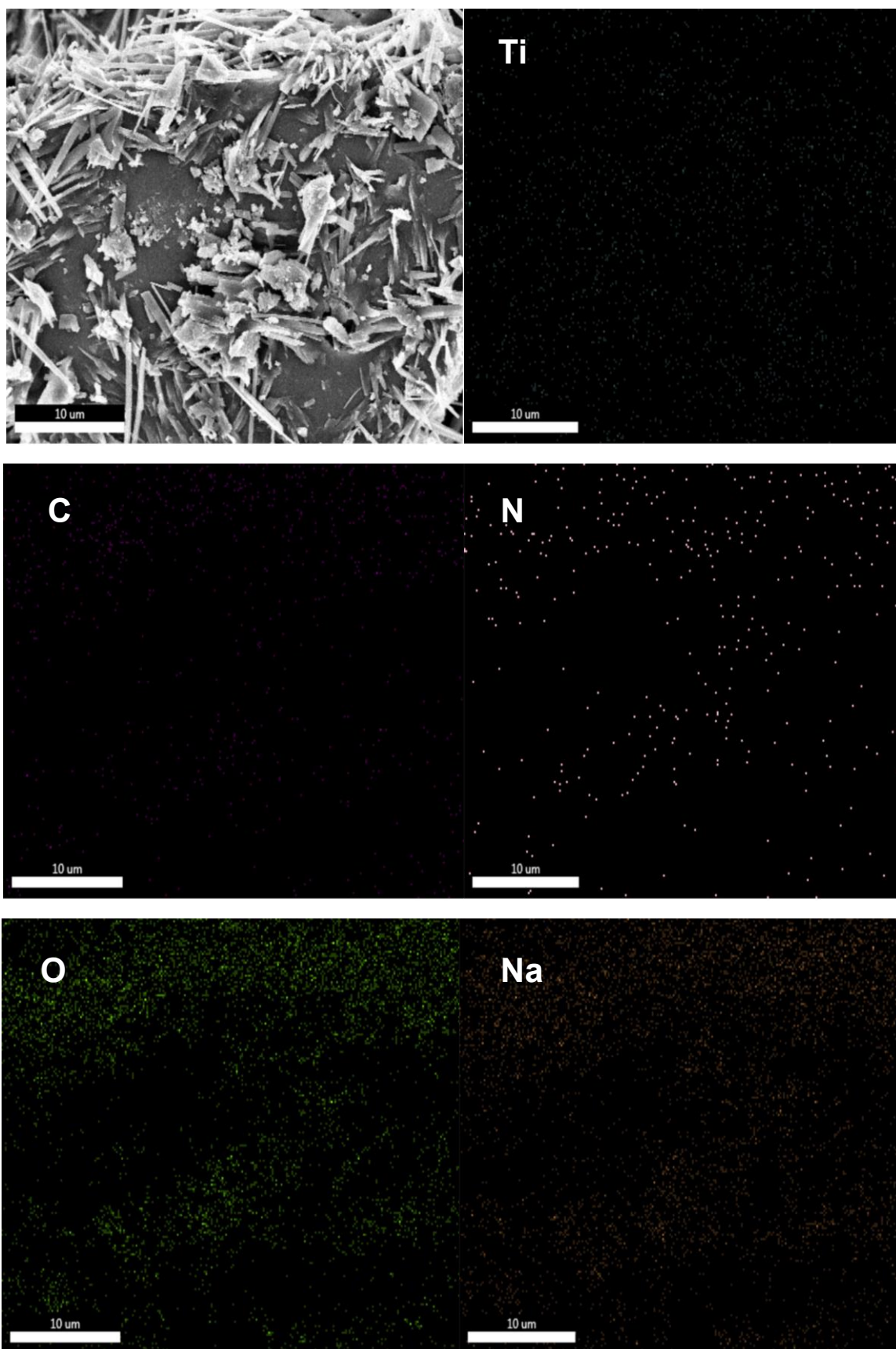


Figure 3-5. SEM mapping images of 1.0 at % EDTA- Na_2/TiO_2 with the elements of Ti, O, N, C, Na.

Table 4: Surface area, pore diameter, pore volume, nitrogen content, and band gap of the modified samples and pristine TiO₂.

	Surface area (m ² /g)	Pore diameter (nm)	Pore volume (cm ³ /g)	% Nitrogen ^a (at %)	Band gap ^b (eV)
Pristine TiO ₂	29	3.6	0.015	0	3.18
0.5 at % EDTA-Na ₂	97	11.8	0.19	0.16	3.15
1.0 at % EDTA-Na ₂	86	13.7	0.35	0.13	2.87
1.5 at % EDTA-Na ₂	59	26.7	0.22	0.05	3.47

^a obtained from the XPS spectra.

^b obtained from the Kubelka – Munk method.

3.3.1.3. Surface area and porosity

Table 4 shows the surface area, pore diameter and pore volume of EDTA-Na₂-modified TiO₂ samples. All modified TiO₂ samples possess higher surface area than the pristine TiO₂, probably due to the formation of a composite structure, which is consistent with the aforementioned SEM and XRD results. Among the modified samples, 0.5 at % EDTA-Na₂/TiO₂ possesses the highest surface area. The surface area significantly decreased with increasing EDTA-Na₂ content, due to partial loss of porosity as a result of the numerous agglomerated TiO₂ particles formed through condensation during the synthesis process.

Fig. 3-6 further shows the porosity of the EDTA-Na₂-modified TiO₂ samples and pristine TiO₂. All isotherms (Fig. 3-6a) possess hysteresis loops which are indicative of mesoporous materials [52]. The hysteresis loop of pristine TiO₂ is an H4-type, which may be attributed to the presence of large mesopores connected to surrounding smaller

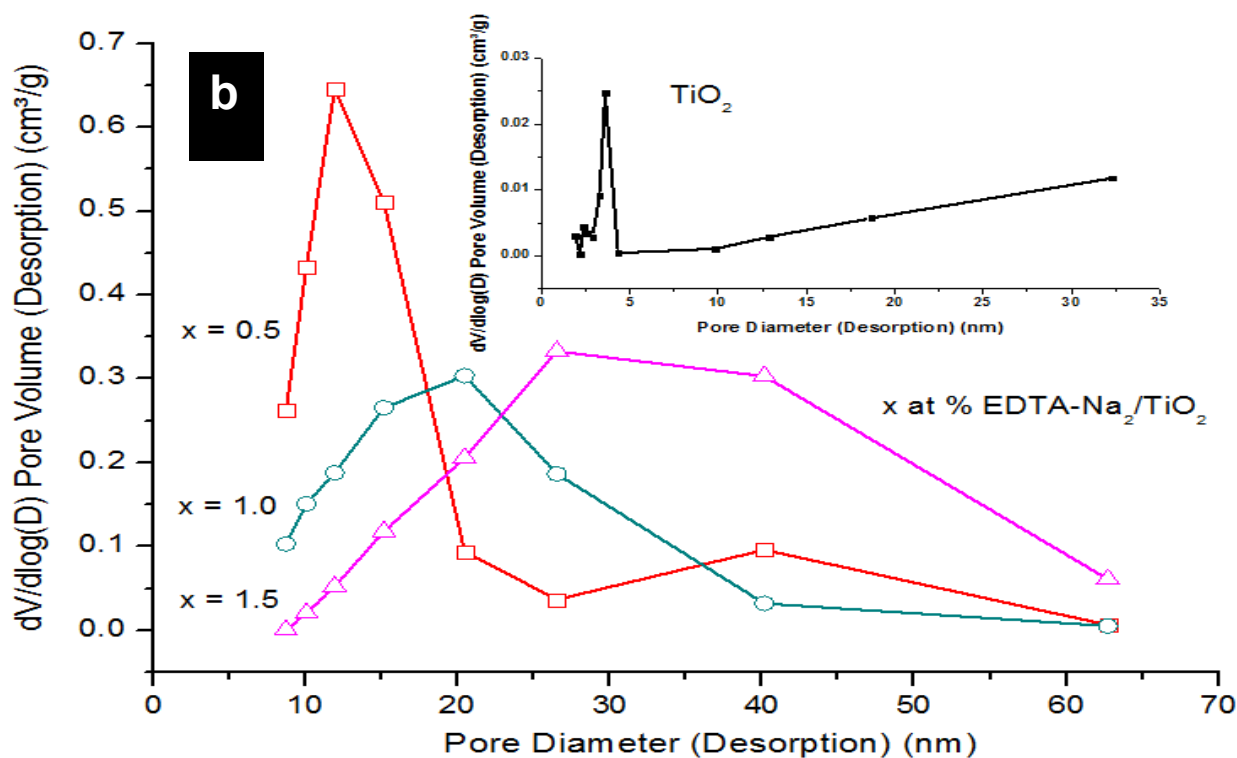
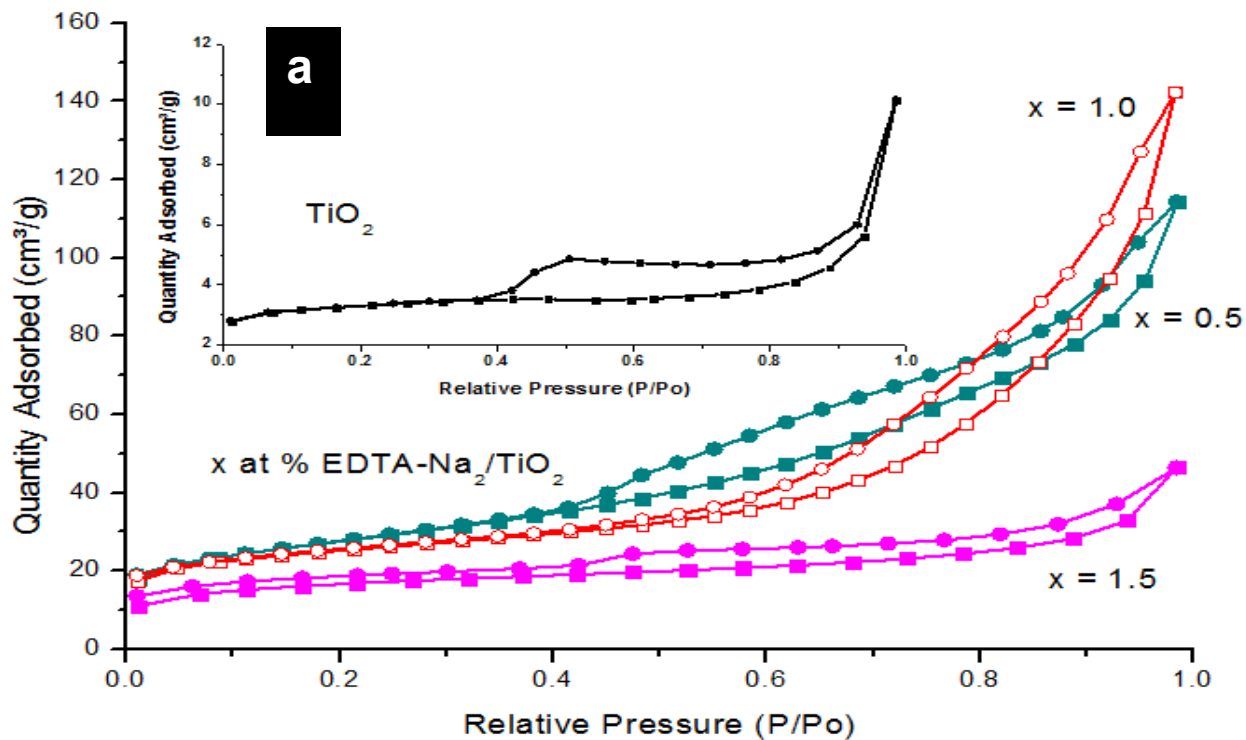


Figure 3-6. (a) Nitrogen adsorption-desorption isotherms and (b) pore size distribution of x at % EDTA-Na₂/TiO₂ (x = 0.5, 1.0, 1.5) and pristine TiO₂.

pores. However, the isotherms of the EDTA- Na_2 -modified TiO_2 % samples show an H3-type hysteresis loop, which indicates cylindrical geometries of mesopores. The significantly late adsorption edges at values of $P/P_0 > 0.8$ indicate an increase in the pore size of the modified samples. Moreover, 0.5 and 1.5 at % EDTA- Na_2/TiO_2 exhibit two-step desorption branches, suggesting either two highest peaks in pore size distribution, or plugs within the pore structure [53]. However, the 1.0 at % EDTA- Na_2/TiO_2 sample displays a smooth desorption branch, leading to a highest peak in pore size distribution. These results are consistent with the pore size distribution shown in Fig. 3-6 (b).

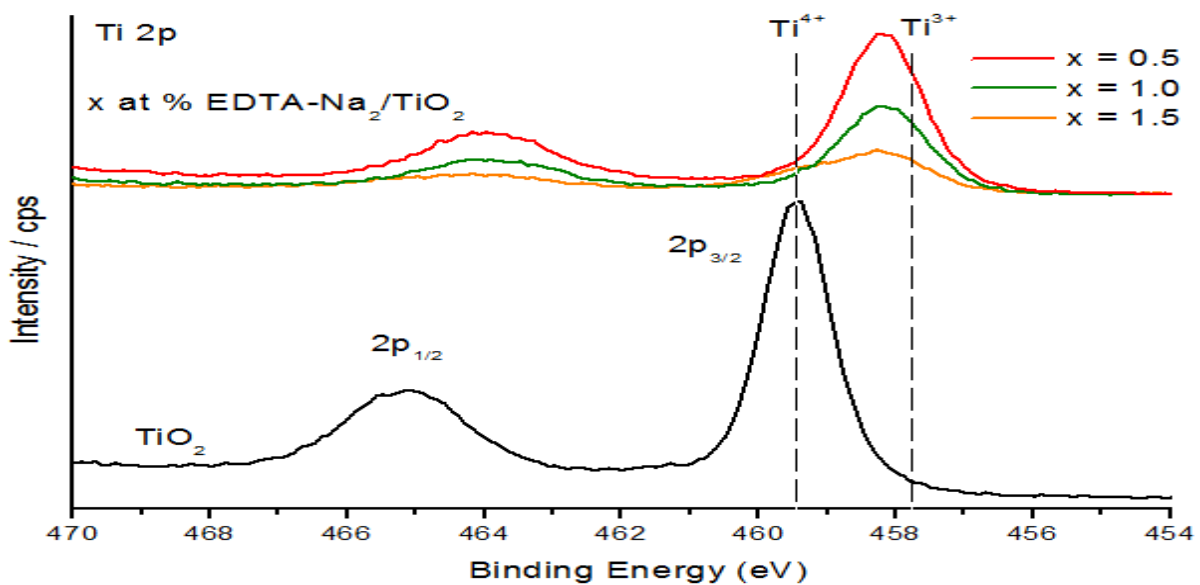


Figure 3-7. XPS spectra details for Ti 2p level of x at % EDTA- Na_2/TiO_2 and pristine TiO_2 .

3.3.1.4. Chemical states

The high resolution Ti 2p spectra of the pristine TiO_2 (Fig. 3-7) show two peaks at 459.4 and 464.8 eV, which represent Ti $2p_{3/2}$ and Ti $2p_{1/2}$ peaks of Ti^{4+} state in pure TiO_2 , respectively.[54] For all modified samples, the ionic states of Ti atoms in this study are determined as a mixture of Ti^{4+} (459.4 eV) and Ti^{3+} (457.9 eV), in which the

Ti³⁺ is dominant [55]. Ti³⁺ was reported to have greater photocatalytic activity than Ti⁴⁺. The lower oxidation states of Ti were attributed to the lattice substitution of N and C dopants for oxygen and titanium, respectively (see N 1s and C 1s XPS spectra in the following paragraphs), and/or the formation of oxygen vacancies during the calcination. Partial substitution of N³⁻ for higher electronegative O²⁻ in the TiO₂ lattice created Ti-N bonds, which increased the electron density around the Ti atoms, and partially reduced the Ti⁴⁺ to Ti³⁺, thus decreasing the binding energies of Ti 2p [56].

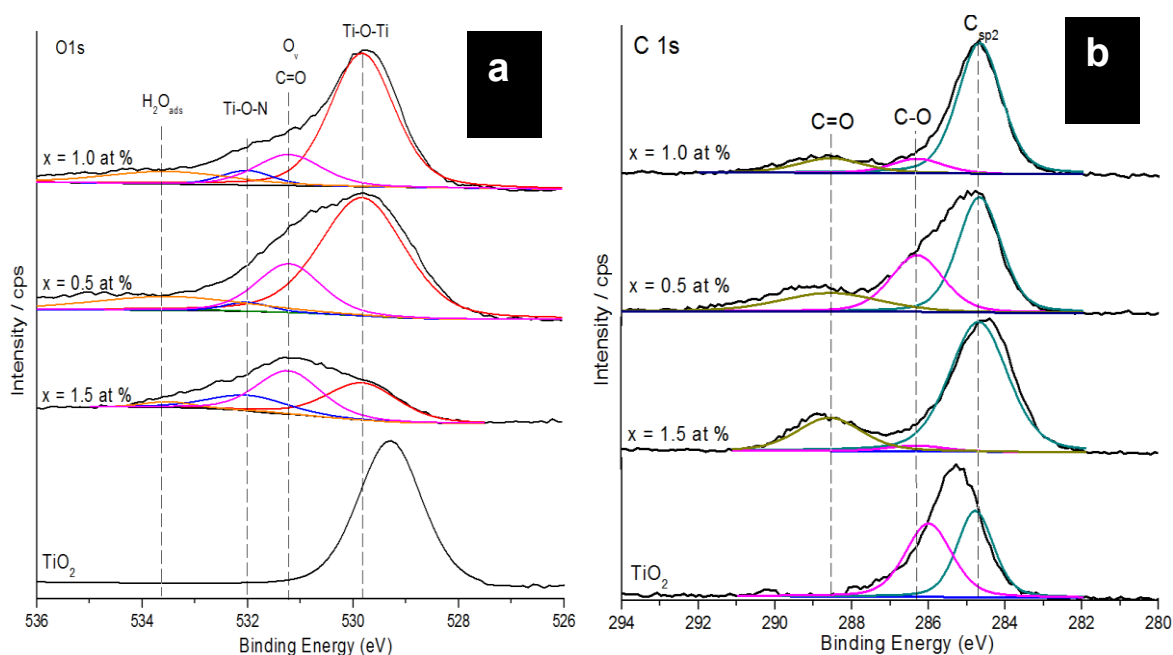


Figure 3-8. XPS spectra details for (a) O 1s level and (b) C 1s level of x at % EDTA-Na₂/TiO₂ and pristine TiO₂.

The O 1s spectra of all modified samples are broader and more asymmetric than that of the pristine TiO₂, indicating complex chemical states of oxygen atoms (Fig. 3-8a). The peak fitting of EDTA-Na₂/TiO₂-modified samples leads to four components at 529.8, 531.2, 532.0, and 533.6 eV, which correspond to Ti-O-Ti, C=O (carbonaceous species) or oxygen vacancies, Ti-O-N linkage, and adsorbed water molecules, respectively [52, 53, 55, 57]. The modified sample with 1.5 at % EDTA-Na₂ has

predominantly adsorbed carbonaceous species on the surface, whereas the other two modified samples have lattice oxygen as a major oxygen component. The increase in carbonaceous species is probably due to the decomposition of excess EDTA-Na₂.

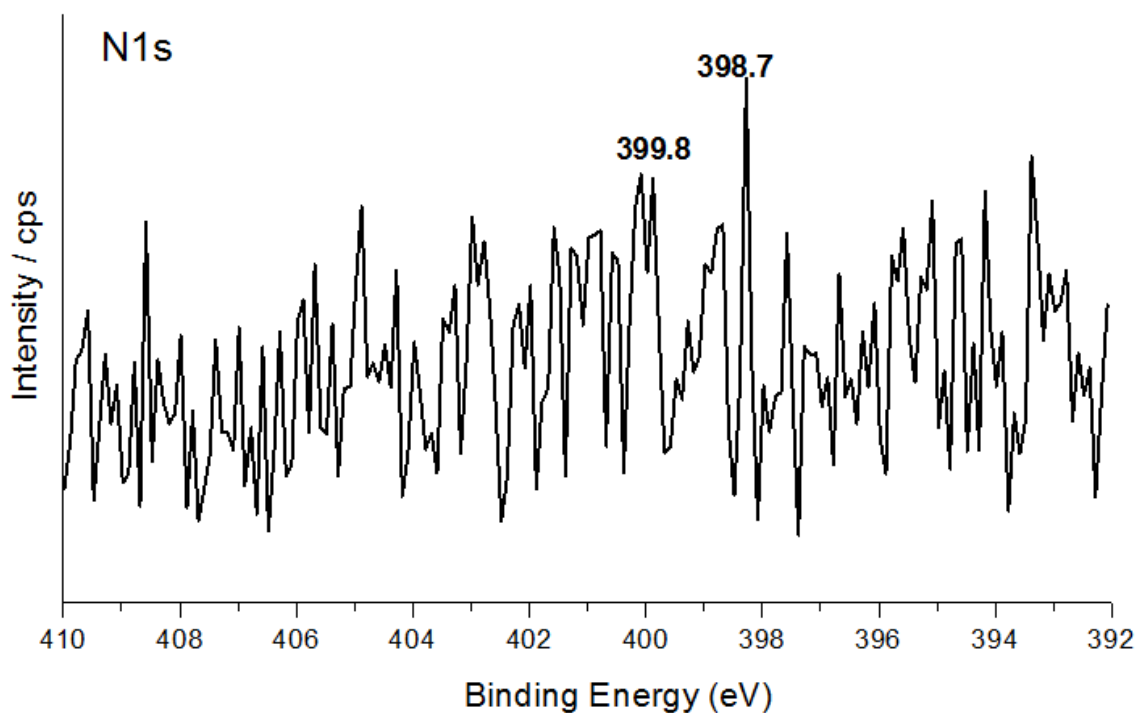


Figure 3-9. XPS spectra details for N 1s level of 1.0 at % EDTA-Na₂/TiO₂.

The core levels of C 1s in Fig. 3-8 (b) further confirmed the formation of carbonaceous species on the surface of the modified samples. The deconvoluted peak at 288.6 eV represents carbonaceous species (C=O bonding) generated during the calcination [58]. The feature at 286.4 eV can be assigned to oxygen-bound species (C-O bonding). It can be inferred that carbonate species may be bound to the TiO₂ surface via C-O-Ti bonds, in which carbon may substitute for some of the lattice titanium atoms. The formation of carbonate species facilitates the charge transfer under visible light irradiation [59]. The most intense peak at 284.6 eV represents adventitious hydrocarbon, which is inevitable for all air-exposed materials.

An increase in EDTA- Na_2 concentration led to a decrease in the nitrogen dopant content (Table 4), probably due to surface and lattice strain relaxation during crystalline srgrowth. The N 1s spectra of 1.0 at % EDTA- Na_2/TiO_2 (Fig. 3-9) revealed interstitial N (Ti-N-O) and substitutional N (N-Ti-O) chemical states at 399.8 and 398.7 eV, respectively [50, 60]. Although the concentration of nitrogen dopants is low, they play a role in significantly enhanced visible light absorption, which was also reported in the literature [61].

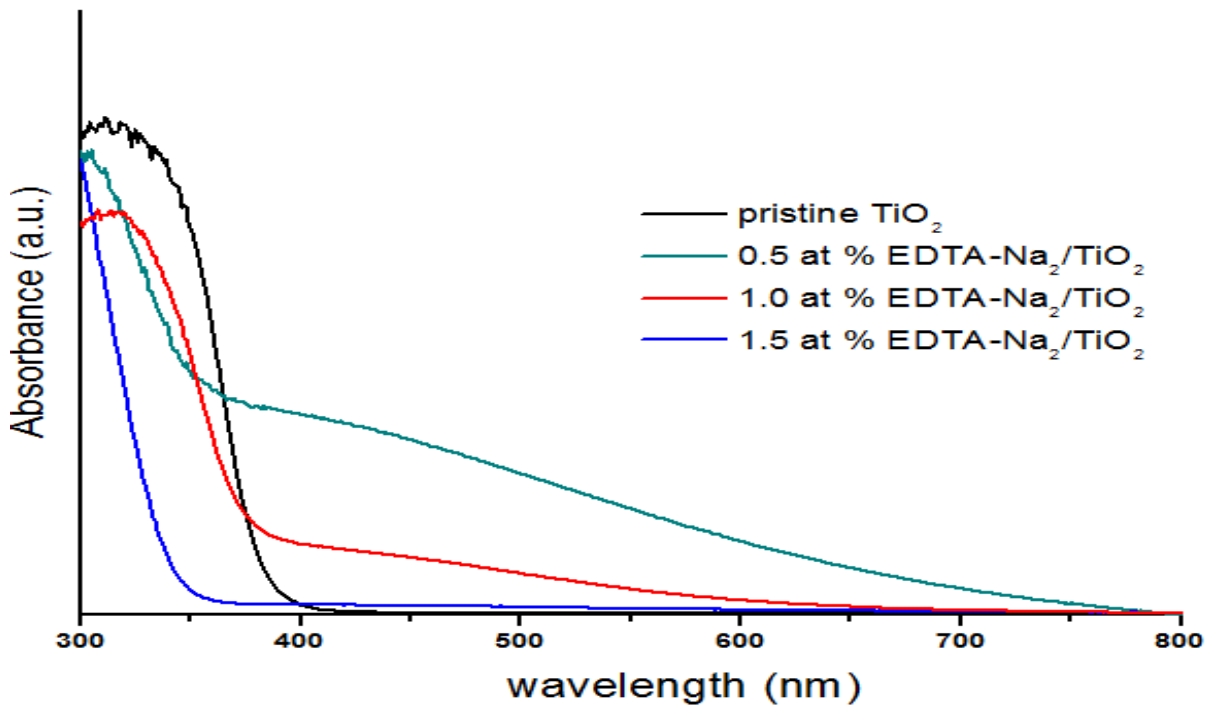


Figure 3-10. UV-vis spectra of the pristine and modified samples.

3.3.1.5. Optical properties

Fig. 3-10 shows that the optical properties of the pristine and as-prepared samples were investigated through the UV-vis diffuse spectra. Compared to the pristine TiO_2 , the modified samples exhibited a weaker absorption in the UV region, indicating the formation of a titanate-anatase heterostructure in the modified samples. No significant visible light absorption was recorded for the pristine TiO_2 , whereas the modified

samples mostly exhibited broad visible absorption. The extended response to the visible range is due to the introduction of nitrogen dopants and Ti^{3+} . The visible light absorption below 550 nm is attributed to the contribution of nitrogen dopants, while the absorption above 550 nm is related to Ti^{3+} [61]. The role of nitrogen dopants in the enhanced visible light absorption is also observed for TiO_2 based materials with extremely low concentration of nitrogen dopants [61]. The incorporation of nitrogen dopants into the TiO_2 lattice can reduce the band gap of the composite by introducing an impurity level above the valence band (VB) of TiO_2 [62]. Owing to the abundance of Ti^{3+} and N dopants among the modified samples, 0.5 at % EDTA- Na_2 / TiO_2 exhibited the strongest visible light absorption. When the EDTA- Na_2 content was increased to 1.5 at %, almost no visible light absorption was observed, indicating that an increase of EDTA- Na_2 does not favor visible light absorption, due to the loss of nitrogen dopants and Ti^{3+} .

3.3.2. The role of EDTA- Na_2

To elucidate the role of EDTA- Na_2 in the formation of titanate-anatase heterojunction, FTIR spectroscopy was used to study the formation of intermediates during the synthesis of the pristine TiO_2 and EDTA- Na_2 modified TiO_2 (Fig. 3-3b). The unmodified xerogel TiO_2 shows the stretching symmetric and antisymmetric C = O vibrations at 1,407 and 1,527 cm^{-1} , respectively. The value of $\Delta\nu$ (C = O) is 120 cm^{-1} , which indicates the bridging structure of acetate titanium complex. The structure of the complex favors the formation of polymers during the condensation of titanium isopropoxides, yielding the formation of anatase titania at 400 °C. The stretching symmetric and antisymmetric of C = O vibrations of the 0.5 at % EDTA- Na_2 modified xerogel TiO_2 were found at 1,401 and 1,634 cm^{-1} , respectively. The value of $\Delta\nu$ (C =

O) is 233 cm^{-1} , which is characteristic of the chelating structure and covalent behavior of the $[\text{Ti}(\text{H}_2\text{O})(\text{EDTA})]$ complex [63]. The complex exists as monomers; therefore, monodispersed particles could be obtained [64]. The employment of EDTA- Na_2 results in altering the condensation pathway of the titanium precursor. Moreover, some of the Ti-O-Ti bonds are broken in the presence of Na^+ , forming layer titanate structures of $\text{Na}_2\text{Ti}_3\text{O}_7$ containing Ti-O-Na by the condensation of TiO_6 octahedral monomers. It is possible that at the same time, acetate titanium complex can also be formed at low ratios of EDTA- Na_2/TiO_2 , which leads to the formation of titanate-anatase composites under heat treatment. Excess EDTA- Na_2 content may prevent TiO_6 octahedra from condensing, yielding the loss of titanate nanorod structure.

EDTA- Na_2 functioned not only as a soft template, but also as a nitrogen source for the synthesis of the heterojunctions. The presence of EDTA- Na_2 during sol-gel generation was responsible for the increase of surface area of the heterojunctions compared to that of the pristine TiO_2 . Also, the photocatalytic activity of the heterojunctions is improved by the doped nitrogen species from EDTA- Na_2 , which is discussed later.

3.3.3. Visible light photocatalytic activity

3.3.3.1. Optimum EDTA- Na_2 content

The photodegradation of MB solution under visible light irradiation was performed to check the photocatalytic activity of the pristine TiO_2 and modified samples. No significant adsorption of MB was observed for pristine TiO_2 (Fig. 3-11).

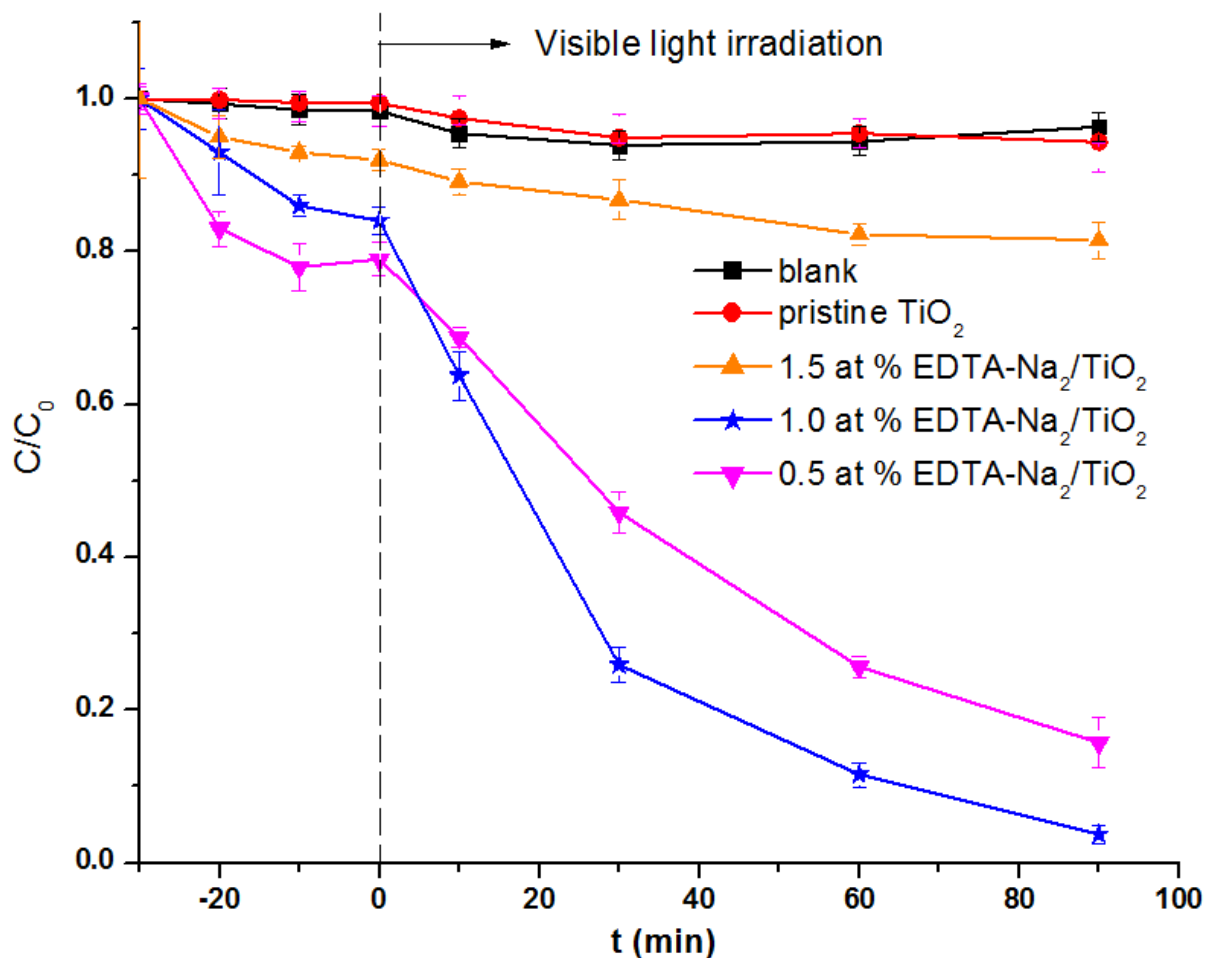


Figure 3-11. Visible light photocatalytic degradation of 20 mL of 10 mg/L MB.

In contrast, all EDTA-Na₂ modified samples have higher adsorption ability. The highest adsorption ability of the 0.5 at % EDTA-Na₂-modified sample was mainly attributed to the high surface area and porosity, which facilitate the adsorption. After the adsorption equilibrium, the light was turned on to monitor the photodegradation of MB of all modified samples. A negligible photolysis of MB was observed under visible light. The same situation was also observed for the pristine TiO₂. Although MB can absorb photons, and its excited electrons can transfer from MB to the conduction band (CB) of TiO₂ due to the greater negative redox potential of its lowest excited state than that of the CB of pristine TiO₂, the photosensitized degradation for pristine TiO₂ was ruled out,

due to no adsorption of MB being observed. The modified samples with 0.5 and 1.0 at % EDTA- Na_2 exhibited a significantly enhanced photoactivity for abating MB in aqueous solution, whereas that with 1.5 at % EDTA- Na_2 revealed negligible photocatalytic activity under visible light.

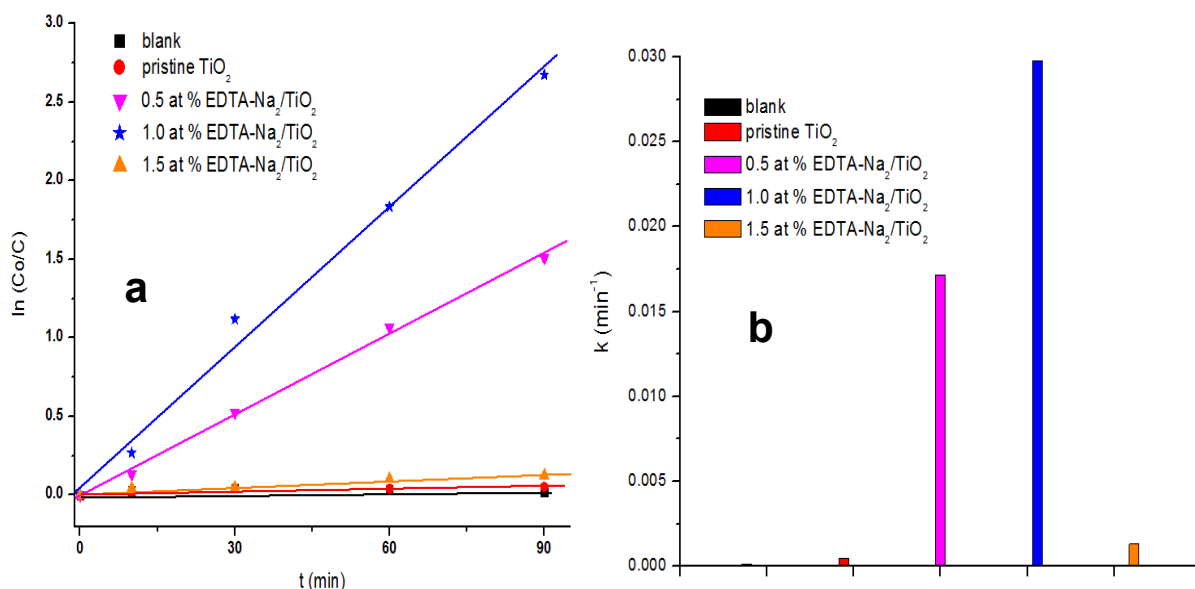


Figure 3-12. Kinetic curves (a) and reaction rate constants (b) for MB degradation over the as-prepared photocatalysts

It was found that the reaction rate constant (k) value of 1.5 at % EDTA- Na_2 (0.00131 min^{-1}) is much lower than those of the 0.5 (0.0172 min^{-1}) and 1.0 at % EDTA- Na_2 (0.0297 min^{-1}) (Fig. 3-12). The photocatalytic degradation of MB was optimized by 1.0 at % EDTA- Na_2 sample, due to the strong suppression of e^-/h^+ recombination and comparative adsorption of MB, which would be discussed later.

3.3.3.2. Luminescence studies

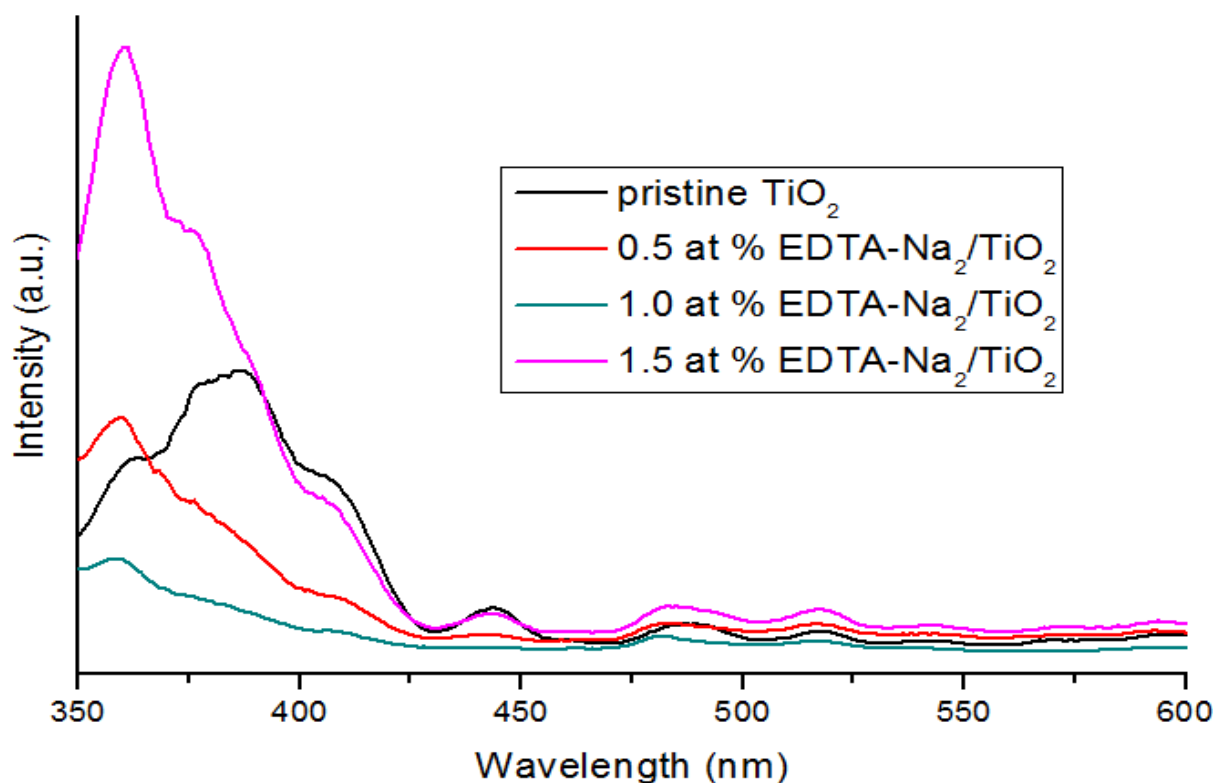


Figure 3-13. PL spectra of pristine and EDTA- Na_2 -modified samples with an excitation wavelength of 325 nm.

Due to the well-known strong correlation between PL intensity and photocatalytic activity, we investigated the effects of different EDTA- Na_2 contents on the photocatalytic activities of the EDTA- Na_2 -modified samples by PL spectroscopy. As the PL emission reflects photo-induced charge recombinations, high intensity PL peaks reveal a high recombination rate, which results in low photocatalytic activity. Fig. 3-13 shows the PL spectra of the pristine and modified samples with an excitation wavelength of 325 nm. The modified samples were also observed to have significantly reduced PL intensity in the visible range compared to that of the pristine TiO_2 , indicating an effective separation of photogenerated e^-/h^+ due to the formation of heterojunctions [65]. The suppression of e^-/h^+ recombination increased with increasing

EDTA-Na₂ content. However, excessive EDTA-Na₂ content induced negative effects of e⁻/h⁺ separation. The results suggest the proper ratio of EDTA-Na₂ and TTIP is required for the effective separation of e⁻ and h⁺. The 1.0 at % EDTA-Na₂/TiO₂ sample exhibited strong suppression of e⁻/h⁺ recombination, leading to the highest photocatalytic activity.

3.3.3.3. Photocatalytic mechanism

To elucidate the photocatalytic mechanism of MB photodegradation, 10.0 mM t-BuOH, BQ and EDTA-Na₂ were used as scavengers of ·OH, ·O₂⁻ and h⁺ species, respectively (Fig. 3-14). The h⁺ and ·OH scavengers showed weak suppression, while the ·O₂⁻ scavenger showed great suppression on the photocatalytic activity of 1.0 at % EDTA-Na₂/TiO₂, indicating that ·O₂⁻ is the dominant radical species for MB photodegradation.

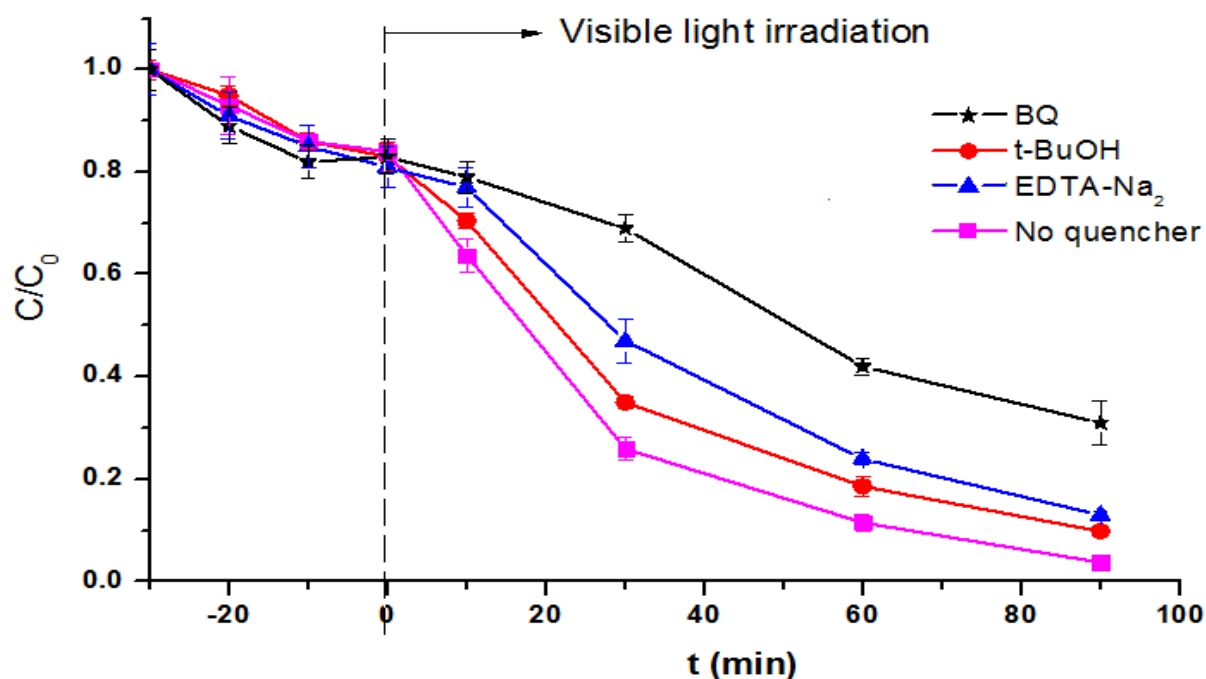
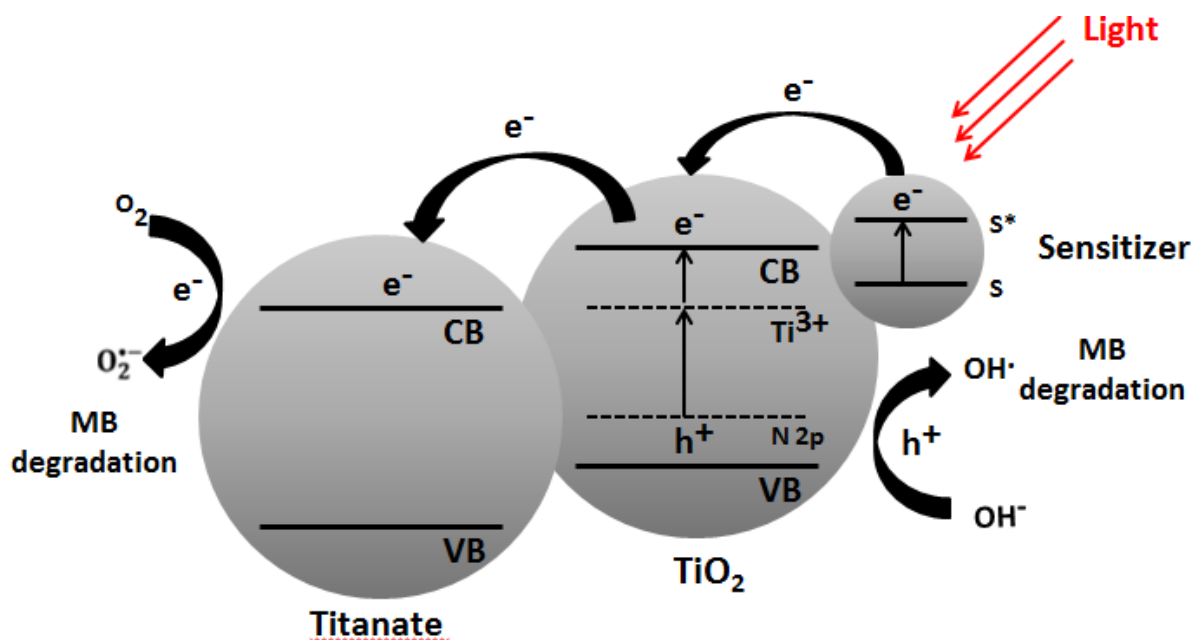


Figure 3-14. MB photocatalytic degradation of 1.0 at % EDTA-Na₂/TiO₂ in the presence of different scavengers.

Scheme 1 illustrates the proposed mechanism of the photodegradation of MB under visible light irradiation. The enhanced photocatalytic activity of the modified samples can be attributed to the synergistic effect of various factors. The effective adsorption of pollutants on the doped TiO₂ can be a prerequisite for improving the photodegradation of pollutants [66]. However, excessive adsorption of MB may prevent the incident light from penetrating into the catalyst, and hence reduce the photocatalytic efficiency of 0.5 at % EDTA-Na₂/TiO₂. Ti³⁺ and nitrogen doping levels can act as e⁻/h⁺ trap centers, which largely reduces the charge recombination. However, the Ti³⁺ defects and N doping sites also act as recombination centers for photogenerated electrons [67]. Therefore, the excess of Ti³⁺ in 0.5 at % EDTA-Na₂/TiO₂ reduced its photocatalytic activity. Meanwhile, interfacial carbonaceous species of the modified samples can act as a photosensitizer that is capable of inserting electrons into the CB of TiO₂, and improving their photocatalytic activity under visible light [68]. Finally, anatase-titanate heterostructure benefits the migration of photo-induced electrons from the CB of TiO₂ to that of Na₂Ti₃O₇, and subsequently to the surface of titanate to react with adsorbed oxygen, producing O₂⁻ and OH· radicals that rapidly attack MB molecules, thus reducing the recombination of electrons and holes.



Scheme 1: The proposed photocatalytic mechanism of the modified catalysts.

3.4. Conclusions

In summary, N-Ti³⁺ codoped mesoporous titanate-TiO₂ rod-like heterojunctions were successfully in-situ synthesized by a one-pot hybridization. The resulting high mesoporosity, low recombination rate of electrons and holes, and effective incorporation of nitrogen dopants and Ti³⁺ defects enhanced the adsorption ability and visible light driven photocatalytic activity in the degradation of MB 10 mg/L. The current photocatalytic system possessed some advantages over other existing titanate-TiO₂ hybrid systems such as more facile fabrication at lower temperature calcination, more effective electron-hole separation, and successful co-doping of Ti³⁺ and nitrogen dopants. This study also proposed photodegradation mechanisms for the removal of dyes under visible light.

CHAPTER 4. EFFECT OF CALCINATION TEMPERATURE ON THE VISIBLE-LIGHT DRIVEN PHOTOCATALYTIC PERFORMANCE OF TITANATE-TiO₂ COMPOSITES

Several studies have reported that the physical and chemical properties of TiO₂-based materials (hierarchical TiO₂-based nanowires[69], rutile TiO₂-based hollow nanorods[70], layered TiO₂-based nanosheets[71], etc.) were strongly dependent on the operational parameters such as the calcination temperature, the reaction time, solution pH and reactant concentration. Particularly, the calcination temperature has a strong effect on the surface morphology, phase composition, crystallinity and photocatalytic activity of TiO₂-based materials.

In the previous chapter, a simple wet chemical method was developed to synthesize visible-light-driven titanate-TiO₂ rod-like composites using ethylenediaminetetraacetic disodium salt (EDTA-Na₂) as both template-directed modifier and nitrogen doping source. Nevertheless, comprehensive investigation has not yet focused on the effect of calcination temperature on the physical properties (surface morphology, crystallinity, optical property and porosity) and visible-light driven photocatalytic performance of TiO₂-titanate heterostructures. Therefore, in this chapter, the influence of the calcination temperature on the physical properties and photocatalytic activity of TiO₂-titanate heterostructures was tested via the degradation of methylene blue (MB) in dark and under visible light.

4.1. Preparation of the composite

4.1.1. Chemicals

EDTA-Na₂ (≥ 99.0 %), acetic acid (≥ 99.7 %), titanium (IV) isopropoxide (TTIP, ≥ 99.99 %), isopropanol (ISP, ≥ 99.7 %), tert-butanol (t-BuOH, ≥ 99.0 %), p-benzoquinone (BQ, ≥ 98 %) and MB (≥ 95.0 %) were purchased from Sigma-Aldrich and were used for experiments without further purification. Deionized (DI) water from a Millipore water (18 MΩ.cm) purification system was used for all experiments.

4.1.2. Preparation method

The same synthesis process as discussed in the previous chapter was applied to this chapter. First, 3.60 g of EDTA-Na₂ was premixed with 100 mL of acetic acid under vigorous stirring at 4 °C for 3 h. A 50.0 mL mixture (1:2) of TTIP and ISP was then added dropwise to the prepared mixture to obtain a suspended solution, which was then placed in the dark for 24 h. The solvent evaporation was performed in a vacuum using a rotary evaporator at 70 °C for 1 h, followed by drying in an oven at 105 °C. The as-prepared samples were then calcined in air at 400, 600 and 800 °C for 3 h with a heating rate of 3 °C/min, and were denoted as TiO₂-BT-400, TiO₂-BT-600 and TiO₂-BT-800, respectively. The samples were ground into powders using a mortar. For comparison, the pristine TiO₂ (without treatment with EDTA-Na₂) was synthesized using the same process and calcined at 400 °C (denoted as TiO₂-400). All reagent-grade chemicals were used without pretreatment.

4.1.3. Characterization

The morphology of the as-synthesized materials was determined by using field emission - scanning electron microscopy (FE-SEM) coupling with energy – dispersive

X-ray (EDX) spectroscopy. The textural properties of the samples, namely the Brunauer-Emmett-Teller (BET) surface area and the pore size, were estimated by N₂ adsorption carried out at -196 °C on a Micromeritics ASAP 2020 analyzer. The pore size distribution was calculated from Barrett-Joyner-Halenda (BJH) desorption branches of isotherms. The crystal phases of the as-synthesized samples were analyzed by X-ray diffraction (XRD) patterns using a Bruker D8 advance powder diffractometer model (Copper anode, working condition: 40kV/ 30mA, scanning type: continuous scanning, $2\theta = 10 - 70^\circ$). The chemical composition of the samples was analyzed based on X-ray photoelectron spectroscopy (XPS) data recorded on a Thermo Scientific Sigma Probe spectrometer with a monochromatic AlK α source (photon energy 1486.6 eV), spot size 400 μm , pass energy of 200 eV and energy step size of 1.0 eV. For high resolution XPS spectra of elemental components, a pass energy of 50 eV and energy step size of 0.10 eV were used. The XPS scanings were conducted in triplicate with an accuracy ± 0.2 eV. For all samples, the C1s peak level was taken as an internal reference at 284.6 eV. All reported binding energy data were taken from high resolution XPS spectra. XPS peaks were deconvoluted by using symmetric Gaussian (Lorentzian) fitting curves. To verify the working optical range of the samples, the UV-vis diffused reflectance spectroscopy (DRS) results of the samples were recorded on a Perkin-Elmer Lambda UV-vis-NIR spectrophotometer. Photoluminescence (PL) spectra were obtained using a PTI luminescence spectrometer with a solid accessory at room temperature. A Genesis 10S UV-Vis spectrophotometer was used to obtain the absorbance of the MB solution at 665 nm.

4.2. Photocatalytic activity test

The same procedure with same photocatalytic reactor as discussed in chapter 3 was conducted. All experiments were triplicated at room temperature. For comparison, the photocatalytic activity of non-porous commercial P25 without further treatment was also checked in the contrast experiment using the same method. For quality assurance and quality control of the measurements, a blank sample (only MB, without catalysts) was subject to the same procedure under identical conditions.

4.3. Results and discussion

4.3.1. Effects of calcination temperature on the physical properties of TiO₂-BTs

4.3.1.1. Morphology

The surface morphologies of TiO₂-400 and TiO₂-BTs were observed and are shown in Fig. 4-1. The top-view SEM image of TiO₂-400 (Fig. 4-1a) revealed the deposition of clusters of nano- to micro-sized particles onto the TiO₂ surface, which was tentatively attributed to the agglomeration of ultrafine TiO₂ powders into larger particles.[50] After heat treatment with EDTA-Na₂, the surface of TiO₂-BT-400 (Fig. 4-1b) clearly shows the presence of irregular rod-like nanostructures, which possessed a heterogenous size distribution with a width of about 140 – 360 nm and a length of 0.7 – 5.0 μm. As the annealing temperature was increased above 600 °C, the nanorod structures totally disappeared (Fig. 4-1c and d), indicating that high annealing temperatures did not favor the formation of nanorod structures. TiO₂-BT-600 and TiO₂-BT-800 had similar surface morphologies to that of TiO₂-400, but the TiO₂-BT-600 surface was more porous than

that of TiO₂-BT-800 was. Obviously, the calcination temperature significantly affected the morphology of TiO₂-BTs.

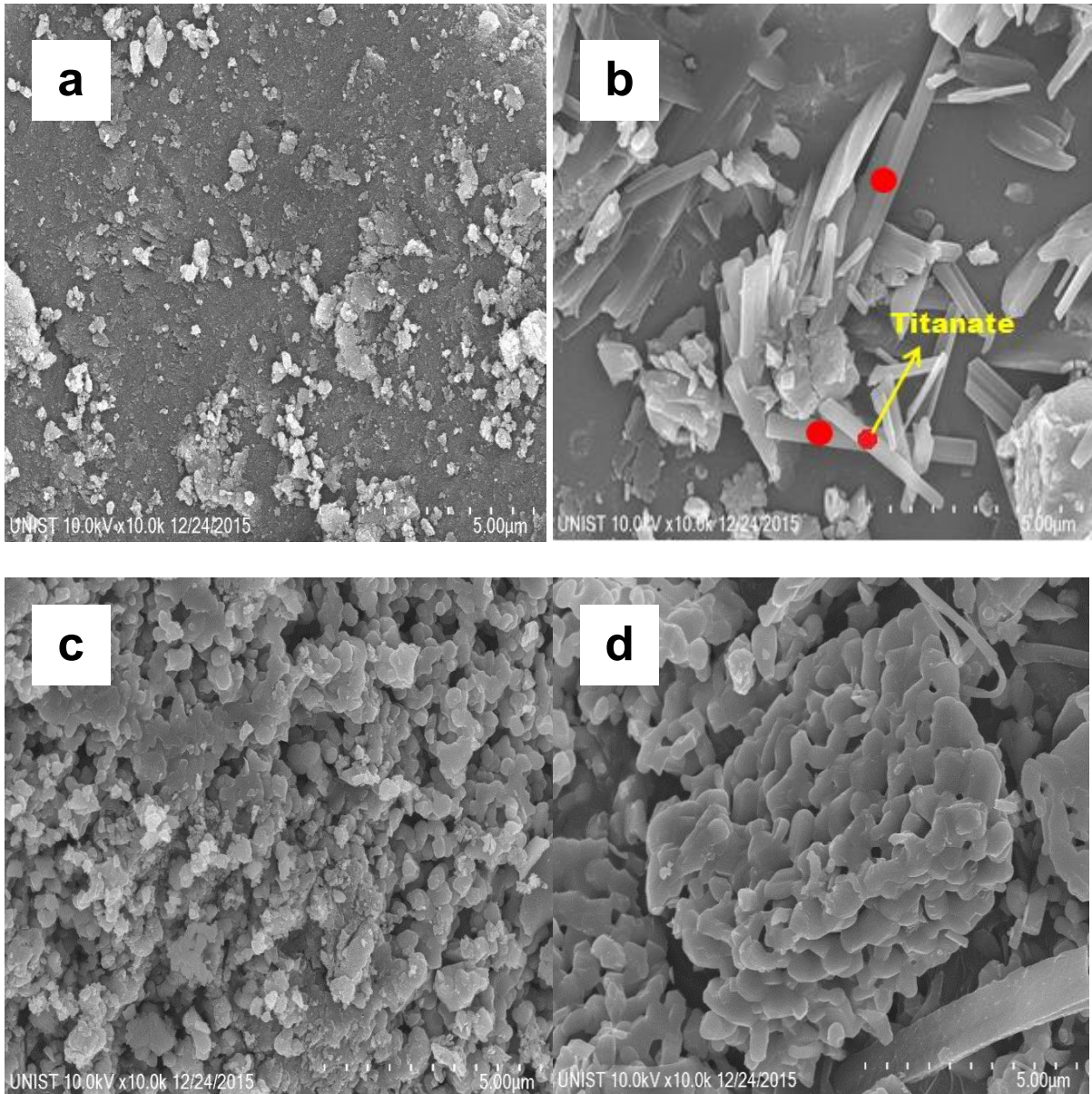


Figure 4-1. FE-SEM images of TiO₂-400 (a) and TiO₂-BT-400, 600, 800 (b, c, d), respectively.

4.3.1.2. Structure analysis

As seen in Fig. 4-2, the XRD pattern of TiO₂-400 exhibited strong characteristic diffraction peaks of anatase [40], suggest a high crystallinity of the anatase phase. A broad peak was also observed for TiO₂-400 at approximately $2\theta = 24^\circ$, which is attributed to the amorphous carbon generating during the calcination.[72] After the heat

treatment with EDTA- Na_2 at different temperatures, more complex XRD patterns were observed for the TiO_2 -BT samples, indicating the existence of a mixture of phase compositions in TiO_2 -BTs. The amorphous carbon was also detected in TiO_2 -BTs. Compared to TiO_2 -400, TiO_2 -BT-400 contained a mixture of anatase and layered titanate $\text{Na}_2\text{Ti}_3\text{O}_7$ (PDF # 31-1329) with a monoclinic lattice (P21/m). The anatase XRD peaks of TiO_2 -BT-400 had a lower intensity than those of TiO_2 -400, indicating their poorer crystallinity.[41] Annealing of TiO_2 -BTs at 600 °C significantly changed their phase composition. No characteristic peaks of anatase were observed for TiO_2 -BT-600. Instead, a mixture of $\text{Na}_2\text{Ti}_3\text{O}_7$ and $\text{Na}_2\text{Ti}_6\text{O}_{13}$ (PDF # 37-0951) was formed. The missing anatase phase and the formation of $\text{Na}_2\text{Ti}_6\text{O}_{13}$ indicate the transformation of anatase into $\text{Na}_2\text{Ti}_6\text{O}_{13}$ in the presence of a significant amount of sodium. The mixture of $\text{Na}_2\text{Ti}_3\text{O}_7$ and $\text{Na}_2\text{Ti}_6\text{O}_{13}$ was retained even after calcination at 800 °C, but with higher crystallinity than that of the mixture obtained at 600 °C. Obviously, the calcination temperature significantly affected the phase composition and crystallinity of TiO_2 -BTs.

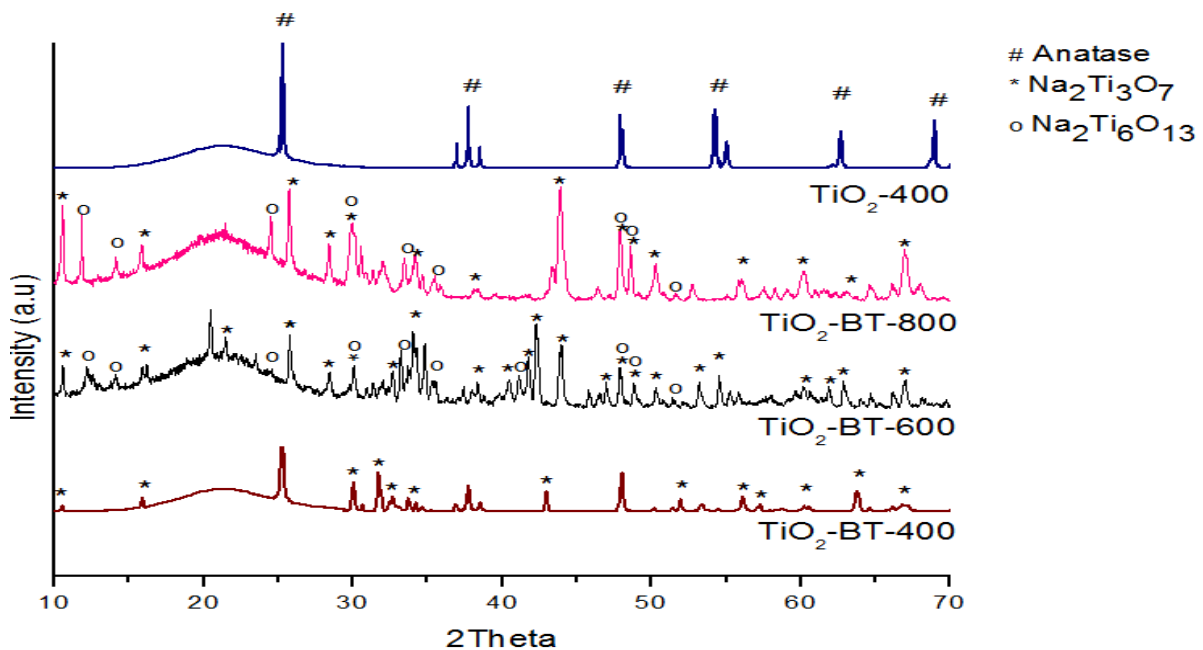


Figure 4-2. XRD patterns of TiO_2 -400 and TiO_2 -BTs.

4.3.1.3. Surface area and porosity

Table 5 shows the surface area, pore diameter and pore volume of TiO₂-400 and TiO₂-BTs. TiO₂-BT-400 had much higher surface area than TiO₂-400 had, probably due to the formation of a composite structure, which is consistent with the aforementioned SEM and XRD results.

Table 5: Surface area, pore diameter, pore volume, nitrogen content and bandgap of TiO₂-400 and TiO₂-BTs.

	Surface area (m ² /g)	Pore diameter (nm)	Pore volume (cm ³ /g)	% Nitrogen ^a (at %)	Bandgap ^b (eV)
TiO ₂ -400	30	3.6	0.015	ND	3.18
TiO ₂ -BT-400	86	13.7	0.35	0.13	2.87
TiO ₂ -BT-600	68	16.6	0.29	ND	3.46
TiO ₂ -BT-800	20	24.3	0.12	ND	3.43

^a obtained from the XPS spectra – ND: Non-detectable

^b obtained from the Kubelka – Munk plots (Fig. 4-7)

At higher annealing temperatures, the loss of heterostructures significantly decreased the surface area and pore volume of TiO₂-BT-600 and TiO₂-BT-800. The pore diameter was increased with increasing annealing temperature for TiO₂-BTs, indicating the presence of interstitial pores and their grain growth. TiO₂-BT-400 had larger pores than TiO₂-400 did at the same calcination temperature because of the larger grain size resulting from the less thermally stable TiO₂ precursor in the presence of EDTA-Na₂.

Fig. 4-3 shows the adsorption-desorption isotherms of TiO₂-400 and TiO₂-BTs for better understanding of porosity. All isotherms possessed hysteresis loops in the relative

range of 0.4-1.0, which is indicative of mesoporous structures.[52] Both TiO₂-400 and TiO₂-BT-600 had H4-type hysteresis loops, which was attributed to the presence of large mesopores surrounded by much smaller pores. The isotherm of TiO₂-BT-400, however, exhibited an H3-type hysteresis loop, which indicates cylindrical geometries of mesopores, whereas that of TiO₂-BT-800 had an H2-type hysteresis loop, which is indicative of the interconnectivity of irregular pores. The adsorption edges at values of $P/P_0 > 0.8$ for isotherms of TiO₂-BTs indicate the larger pores of TiO₂-BTs. Obviously, the surface area and pore structures of TiO₂-BTs were strongly influenced by heating temperature: the increase of calcination temperature resulted in the collapse of porosity and the decrease in surface area of the porous TiO₂-BTs.

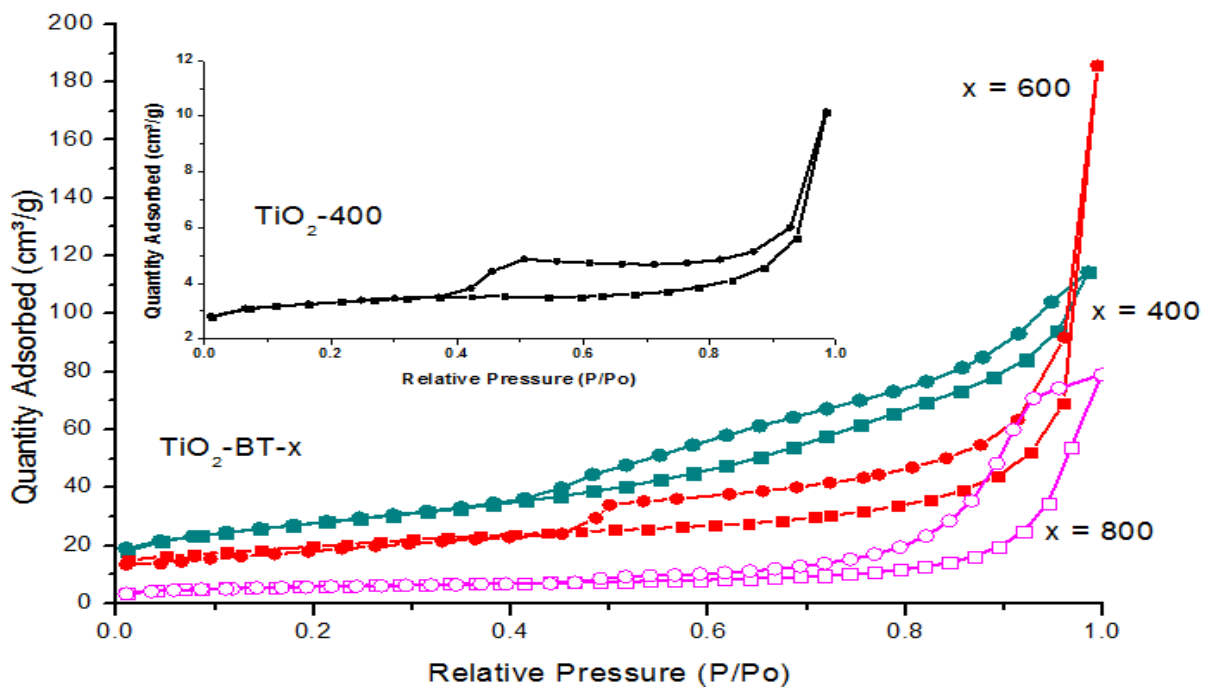


Figure 4-3. Nitrogen adsorption-desorption isotherms of TiO₂-400 (inset) and TiO₂-BTs.

4.3.1.4. Chemical states

XPS was carried out to examine the surface composition and chemical states of elements in TiO₂-400 and TiO₂-BTs. Fig. 4-4a shows the C 1s spectra of TiO₂-BTs with

three deconvoluted peaks. The most intense peak at 284.6 eV represents adventitious hydrocarbon, which is inevitable for all air-exposed materials, while the other two peaks at 286.4 eV and 288.6 eV mostly correspond to oxygen-bound species (C-O bonding) and carbonaceous species (C=O bonding) generated during the calcination, respectively.[58] It can be inferred that carbonate

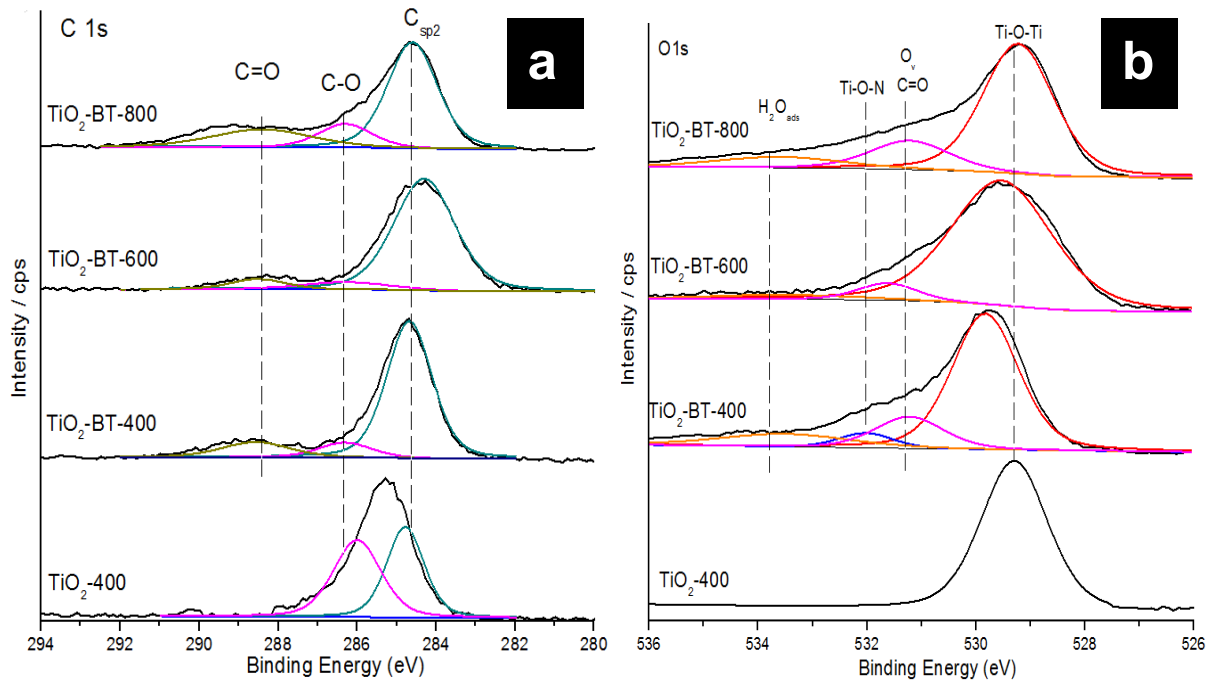


Figure 4-4. XPS spectra details for (a) C 1s level and (b) O 1s level of TiO₂-400 and TiO₂-BTs.

species may be bound to the TiO₆ octahedra surface via C-O-Ti bonds in which carbon may substitute for some of the lattice titanium atoms. The formation of carbonate species could promote the charge transfer under visible light excitation.[59] An increase in calcination temperature decreased the nitrogen content (Table 5) due to the loss of the nitrogen dopant species formed through the decomposition of Ti-EDTA complex at higher temperatures (above 400 °C). No nitrogen dopants were observed for TiO₂-BT-600 and TiO₂-BT-800. The N 1s spectra of TiO₂-BT-400 (Fig. 4-5) revealed chemical states of interstitial N (Ti-N-O) and substitutional N (N-Ti-O) dopants into the TiO₆

octahedra lattice, which were observed at 399.8 eV and 398.7 eV, respectively.[52] The presence of N dopants in TiO₂-BT-400 was also detected in its SEM mapping images (Fig. 3-5) and O 1s XPS spectra. Although their concentration was quite low (0.15 at %), they still played a role in significantly enhanced visible light absorption, which was also reported in the literature.[61]

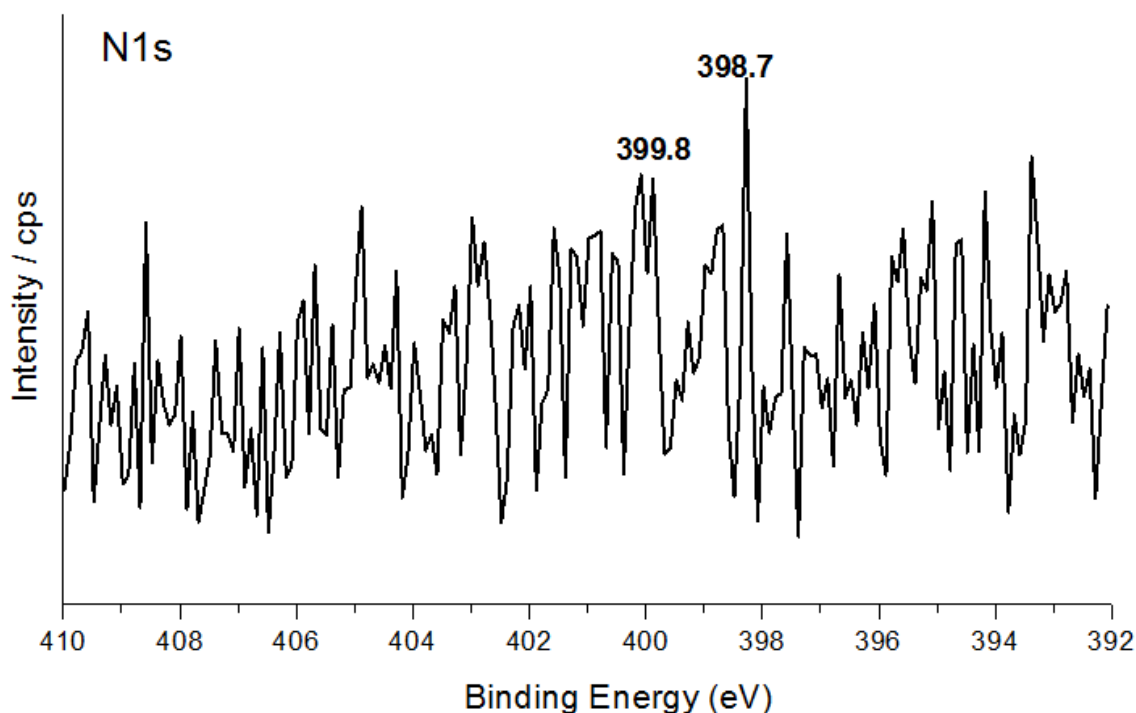


Figure 4-5. XPS spectra details for N 1s level of TiO₂-BT-400.

For TiO₂-400, the high resolution XPS spectra of Ti 2p (Fig. 4-6) reveal the contribution of two typical Ti 2p_{3/2} and Ti 2p_{1/2} peaks of pure TiO₂ at 459.4 eV and 464.8 eV, respectively.[52] For TiO₂-BTs, two typical Ti 2p peaks reveal a large shift of about 1.5 - 1.9 eV towards lower binding energies, indicating the coexistence of the more electronegative states (Ti³⁺ or Ti²⁺) of Ti rather than only the Ti⁴⁺ state. The binding energies for Ti³⁺ and Ti²⁺ were reported at 457.8 eV and 456.2 eV, respectively.[55] Accordingly, the ionic states of Ti atoms for TiO₂-BTs should have been a mixture of Ti⁴⁺ (459.4 eV) and Ti³⁺ (457.9 eV), in which the Ti³⁺ chemical state

was dominant. The red shift intensity was increased with increasing annealing temperature, indicating that the formation of the Ti^{3+} ionic state was favorable at high temperatures (above 400 °C). Ti^{3+} has greater photocatalytic activity than Ti^{4+} has. The red shift of Ti^{4+} to lower chemical states was ascribed to the incorporation of N (for $\text{TiO}_2\text{-BT-400}$) and C dopants into the TiO_6 octahedra lattice, and/or the formation of oxygen vacancies during the calcination. Partial substitution of N^{3-} for more electronegative O^{2-} in the TiO_6 octahedra lattice creates Ti-N bonds, which increases the electron density around the Ti atoms and partially reduces Ti^{4+} to Ti^{3+} ; thus, the substitution reflects a decrease in binding energies of Ti 2p. The same effects were also observed when Ti-O-C bonds were formed on the TiO_6 octahedra surface.[56] The O 1s spectra of $\text{TiO}_2\text{-BTs}$ were broader and more asymmetric than those of $\text{TiO}_2\text{-400}$, indicating the presence of more than one valence state of O atoms based on the binding energy (Fig. 4-4b). The peak fitting of $\text{TiO}_2\text{-BT-400}$ led to four components at 529.8, 531.2, 532.0 and 533.6 eV, which were assigned to Ti-O-Ti (lattice O), C=O (carbonaceous species) or oxygen vacancies, Ti-O-N linkage (interstitial N) and adsorbed water molecules, respectively [52, 53, 55, 57]. An increase in calcination temperature resulted in the loss of nitrogen dopants for $\text{TiO}_2\text{-BT-600}$ and $\text{TiO}_2\text{-BT-800}$.

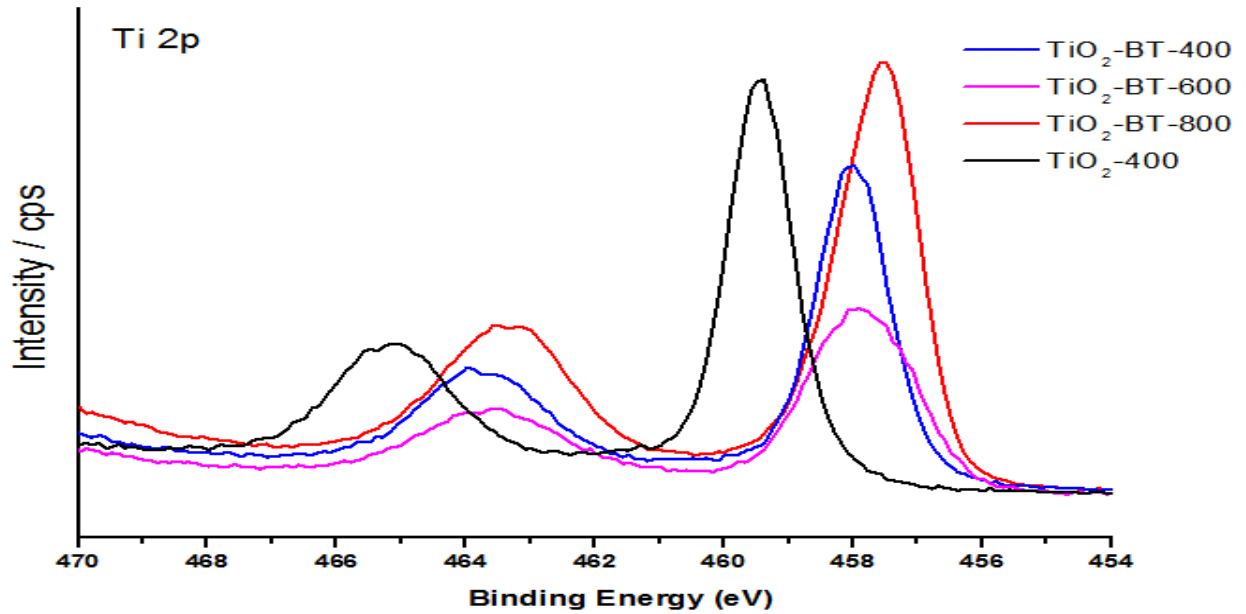


Figure 4-6. XPS spectra details for Ti 2p level of TiO₂-400 and TiO₂-BTs.

4.3.1.5. Optical properties

The optical properties of TiO₂-400 and TiO₂-BTs were studied through the UV-vis diffuse spectra, as shown in Fig. 4-7. The apparent bandgaps of TiO₂-BTs are listed in Table 5. Accordingly, there is no discrepancy in the band gaps of TiO₂-BT-600 and TiO₂-BT-800 due to the similarity in structural composition of the samples after calcination at 600 °C.

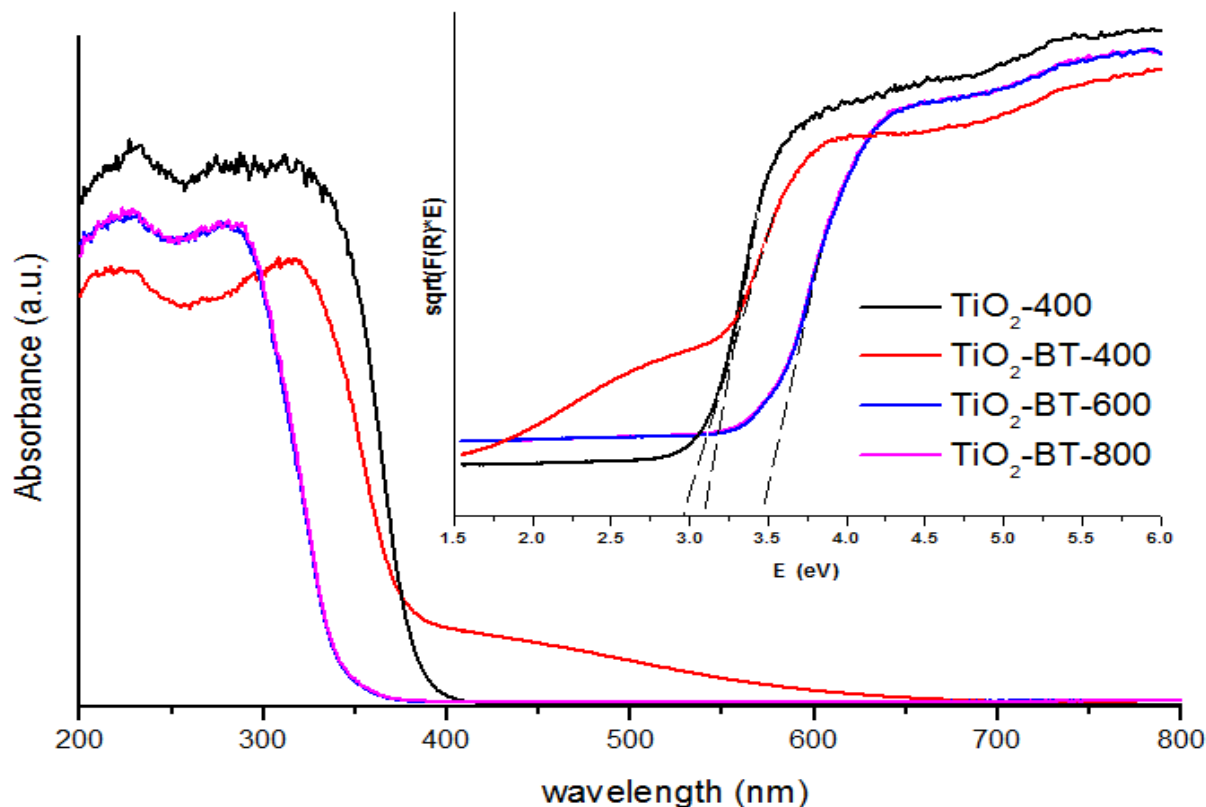


Figure 4-7. UV-vis spectra and Kubelka – Munk plots (inset) of TiO₂-400 and TiO₂-BTs.

While no visible light absorption was observed for either TiO₂-400, TiO₂-BT-600 or TiO₂-BT-800, TiO₂-BT-400 was significantly absorbing in the visible range. The visible light harvesting of TiO₂-BT-400 was associated with the effects of both nitrogen dopants and Ti³⁺ species. The absorption in the visible range below 550 nm was ascribed to the effect of nitrogen dopants, and that above 550 nm to that of Ti³⁺. [73] The incorporation of Ti³⁺ and nitrogen dopants into the TiO₆ octahedra lattice of TiO₂-BT-400 can narrow the optical bandgap of TiO₂ by introducing localized midgap states below the conduction band (CB) and above the valence band (VB) of TiO₂, respectively. [68] As there is weak absorption above 550 nm, the enhanced visible light absorption ability was mainly related to the introduction of N dopants. Although the formation of Ti³⁺ chemical states was also recorded for TiO₂-BT-600 and TiO₂-BT-800,

no visible light absorption was observed due to the wide bandgap of $\text{Na}_2\text{Ti}_3\text{O}_7$ (3.54 eV) and $\text{Na}_2\text{Ti}_6\text{O}_{13}$ (3.44 eV).[74] Obviously, calcination of TiO_2 -BTs at low temperature ($< 600\text{ }^\circ\text{C}$) significantly affected the optical properties of TiO_2 -BTs.

4.3.2. Effects of calcination temperature on the photocatalytic activity of TiO_2 -BTs under visible light.

The photodegradation of MB in aqueous solution under visible light irradiation was investigated to study the photocatalytic activity of P25, TiO_2 -400 and TiO_2 -BTs at room temperature. Prior to the irradiation with visible light, the adsorption of all tested samples was conducted in the dark condition for 30 mins to attain equilibrium. No significant adsorption of MB was observed for P25, TiO_2 -400 and TiO_2 -BT-800 (Fig. 4-8).

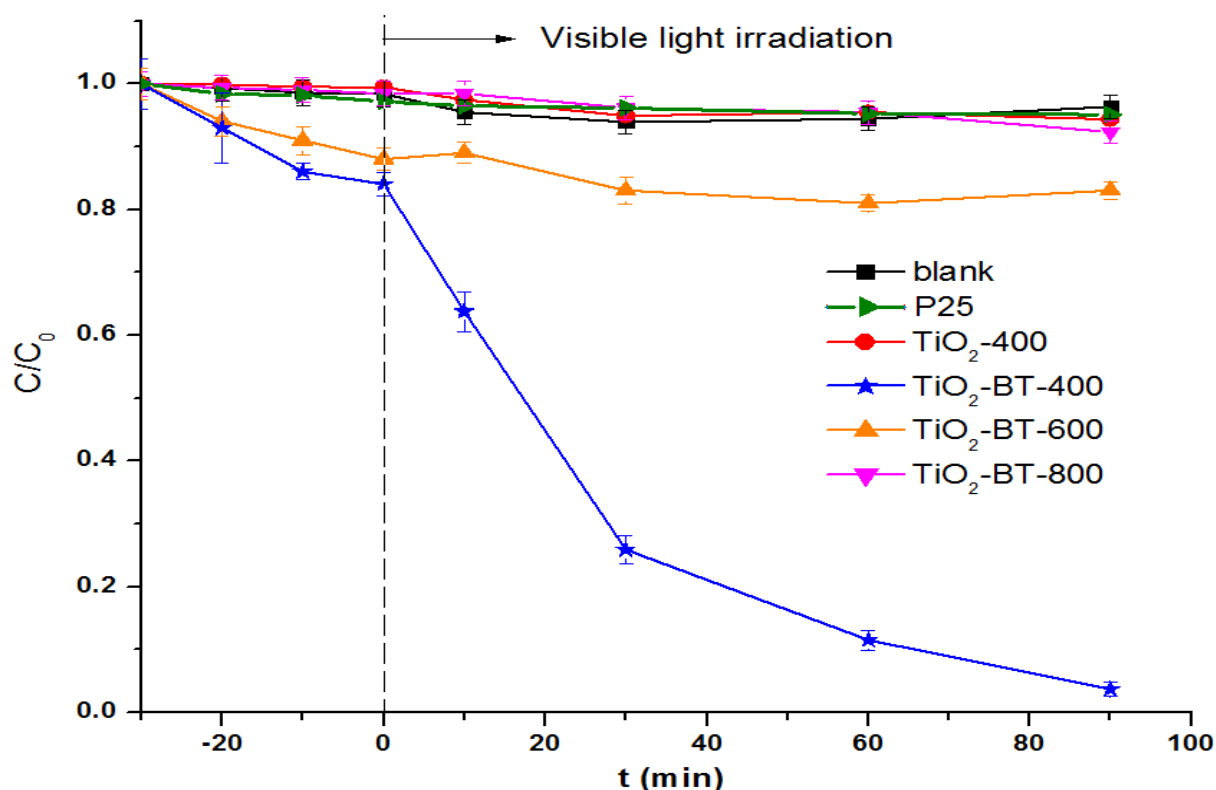


Figure 4-8. Photocatalytic degradation of 20 mL of 10 mg/L MB under visible light in 2 h by using 20 mg of TiO_2 -400 and TiO_2 -BTs. A blank sample (without any catalysts) was also used for comparison.

In contrast, TiO₂-BT-400 and TiO₂-BT-600 exhibited higher MB adsorption ability due to their better textural properties. The highest adsorption ability of TiO₂-BT-400 was mainly attributed to its largest area, which facilitates the adsorption. Under visible light irradiation, TiO₂-400 showed negligible decoloration of MB. Although MB can absorb photons and its excited electrons can transfer from MB to the CB of TiO₂ due to its more negative redox potential of the lowest excited state than the CB of TiO₂-400, the photosensitized degradation for TiO₂-400 was ruled out due to the absence of any observed adsorption of MB. Therefore, the negligible decoloration of MB under visible light was related to the photolysis of MB. The negligible decoloration of MB via the photolysis was also observed for P25, TiO₂-BT-600 and TiO₂-BT-800. TiO₂-BT-400, however, showed a significantly enhanced photodegradation of MB. About 88% of 10 mg/ L MB solution was removed from aqueous solution after 90 mins of visible light irradiation.

4.4. Conclusions

The obtained rod-like heterostructures were thermally less stable at high temperatures (> 400 °C). The Na₂Ti₃O₇ – anatase rod-like heterostructure underwent structural conversion into the Na₂Ti₃O₇- Na₂Ti₆O₁₃ heterostructure at calcination temperatures higher than 400 °C. The photocatalytic activity of the rod-like heterostructures under visible light irradiation was also significantly affected by the calcination temperature. The rod-like heterostructures, which resulted from low calcination temperature (~ 400 °C), exhibited enhanced visible light photocatalytic activity in the degradation of 10 mg/L MB. The high calcination temperatures of the rod-like heterostructures (> 400 °C)

afforded materials that were inactive under visible light. The enhanced photocatalytic activity of the heterostructures was attributed to their high mesoporosity, low recombination rate of electrons and holes, and effective incorporation of nitrogen dopants and Ti^{3+} defects. The current photocatalytic system possessed some advantages over other existing titanate- TiO_2 hybrid systems such as more facile fabrication at lower temperature calcination, more effective electron-hole separation, and successful co-doping of Ti^{3+} and nitrogen dopants.

CHAPTER 5. CONCLUSION AND FUTURE STUDY PLAN

- ✓ The synthesis method is simply performed in lab-scaled environment.
- ✓ The synthesized material could work as either or both of photocatalysts and adsorbents for removal of organic dyes from aqueous solutions.

Gaps in this study are inevitable. This study lacks of the followings for a better quality:

- Not only methylene blue but also other types of dyes or other pollutants should be investigated as testing pollutants.
- The visible light absorption ability of TiO_2 could be potentially enhanced further by other methods.
- The immobilization of the material on suitable substrates is needed for real application due to the difficulty in removing the modified TiO_2 from aqueous phase after treatment.

REFERENCES

- [1] D. Li, X. Cheng, X. Yu, Z. Xing, *Chem. Eng. J.* 279 (2015) 994-1003.
- [2] V. Binas, D. Venieri, D. Kotzias, G. Kiriakidis, *J. Jmat* 3 (2017) 3-16.
- [3] M. Sohail, H. Xue, Q. Jiao, H. Li, K. Khan, S. Wang, Y. Zhao, *Mater. Res. Bull.* 90 (2017) 125-130.
- [4] W.C. Huang, J.-M. Ting, *Ceram. Int.* 43 (2017) 9992-9997.
- [5] Z. Xiong, X.S. Zhao, *J. Am. Chem. Soc.* 134 (2012) 5754-5757.
- [6] Z. Meng, L. Wang, X. Li, G. Zhang, H. Li, *Int. J. Hydrogen Energy* 42 (2017) 2177-2186.
- [7] D. Zhang, X. Zhang, X. Ni, J. Song, H. Zheng, *Cryst. Growth Des.* 7 (2007) 2117-2119.
- [8] C. Li, J. Yang, P. Yang, X. Zhang, H. Lian, J. Lin, *Cryst. Growth Des.* 8 (2008) 923-929.
- [9] L.-P. Wang, L.-M. Chen, *Mater. Charact.* 69 (2012) 108-114.
- [10] D. Nassoko, Y.-F. Li, H. Wang, J.-L. Li, Y.-Z. Li, Y. Yu, *J. Alloys Compd.* 540 (2012) 228-235.
- [11] D. Ensor, *Aerosol science and technology: History and reviews*, RTI Press Research Triangle Park, NC: RTI Press, 2011.
- [12] K. Hashimoto, H. Irie, A. Fujishima, *Jpn. J. Appl. Phys.* 44 (2005) 8269-8285.
- [13] M. Pelaez, N.T. Nolan, S.C. Pillai, M.K. Seery, P. Falaras, A.G. Kontos, P.S.M. Dunlop, J.W.J. Hamilton, J.A. Byrne, K. O'Shea, M.H. Entezari, D.D. Dionysiou, *Appl. Catal., B* 125 (2012) 331-349.

- [14] G.L. Amy L. Linsebigler, John T. Yates, Jr., *Chem. Rev.* 95 (1995) 735-758.
- [15] X. Yu, S. Liu, J. Yu, *Appl. Catal., B* 104 (2011) 12-20.
- [16] C. Fernández-Rodríguez, J.M. Doña-Rodríguez, O. González-Díaz, I. Seck, D. Zerbani, D. Portillo, J. Perez-Peña, *Appl. Catal., B* 125 (2012) 383-389.
- [17] A.G. Agrios, P. Pichat, *J. Photochem. Photobiol., A* 180 (2006) 130-135.
- [18] J. Chen, F. Qiu, W. Xu, S. Cao, H. Zhu, *Appl. Catal., A* 495 (2015) 131-140.
- [19] H. Zangeneh, A.A.L. Zinatizadeh, M. Habibi, M. Akia, M. Hasnain Isa, *J. Ind. Eng. Chem.* 26 (2015) 1-36.
- [20] X. Zhang, X. Li, Q. Zhang, J. Yang, N. Deng, *Catal. Commun.* 16 (2011) 7-10.
- [21] Z.L. Wang, *Mater. Today* 10 (2007) 20-28.
- [22] S.-x. Li, F.-y. Zheng, X.-l. Liu, F. Wu, N.-s. Deng, J.-h. Yang, *Chemosphere* 61 (2005) 589-594.
- [23] Ş. Neaţu, J.A. Maciá-Agulló, P. Concepción, H. Garcia, *J. Am. Chem. Soc.* 136 (2014) 15969-15976.
- [24] X. Li, G. Wang, X. Li, D. Lu, *Appl. Surf. Sci.* 229 (2004) 395-401.
- [25] S. Xu, L. Gu, K. Wu, H. Yang, Y. Song, L. Jiang, Y. Dan, *Sol. Energy Mater. Sol. Cells* 96 (2012) 286-291.
- [26] J. Senthilnathan, L. Philip, *Chem. Eng. J.* 161 (2010) 83-92.
- [27] D.V. Šojić, V.N. Despotović, N.D. Abazović, M.I. Čomor, B.F. Abramović, *J. Hazard. Mater.* 179 (2010) 49-56.
- [28] D. Li, Z. Chen, Y. Chen, W. Li, H. Huang, Y. He, X. Fu, *Environ. Sci. Technol.* 42 (2008) 2130-2135.

- [29] J.C. Yu, W. Ho, J. Yu, H. Yip, P.K. Wong, J. Zhao, *Environ. Sci. Technol.* 39 (2005) 1175-1179.
- [30] P. Wu, R. Xie, K. Imlay, J.K. Shang, *Environ. Sci. Technol.* 44 (2010) 6992-6997.
- [31] K.S.W. Sing, D.H. Everett, R.A.W. Haul, L. Moscou, R.A. Pierotti, J. Rouquerol, T. Siemieniewska, *Reporting Physisorption Data for Gas/Solid Systems, Handbook of Heterogeneous Catalysis*, Wiley-VCH Verlag GmbH & Co. KGaA, 2008.
- [32] J.C.P. Broekhoff, *Mesopore Determination from Nitrogen Sorption Isotherms: Fundamentals, Scope, Limitations*, Elsevier, 1979.
- [33] X.S. Zhao, G.Q. Lu, G.J. Millar, *Ind. Eng. Chem. Res.* 35 (1996) 2075-2090.
- [34] D. Shooter, *AIChE J.* 22 (1976) 202-202.
- [35] Z. AlOthman, *Materials* 5 (2012) 2874-2902.
- [36] H. Ali, *Water, Air, Soil Pollut.* 213 (2010) 251-273.
- [37] M.T. Yagub, T.K. Sen, S. Afroze, H.M. Ang, *Adv. Colloid Interface Sci.* 209 (2014) 172-184.
- [38] M.A.M. Salleh, D.K. Mahmoud, W.A.W.A. Karim, A. Idris, *Desalination* 280 (2011) 1-13.
- [39] Y.H. Cheng, Y. Huang, P.D. Kanhere, V.P. Subramaniam, D. Gong, S. Zhang, J. Highfield, M.K. Schreyer, Z. Chen, *Chem. - Eur. J.* 17 (2011) 2575-2578.
- [40] A.L. Sauvet, S. Baliteau, C. Lopez, P. Fabry, *J. Solid State Chem.* 177 (2004) 4508-4515.
- [41] P. Zhang, C. Shao, Z. Zhang, M. Zhang, J. Mu, Z. Guo, Y. Liu, *Nanoscale* 3 (2011) 2943-2949.

- [42] X. Chen, L. Liu, P.Y. Yu, S.S. Mao, *Science* 331 (2011) 746-750.
- [43] S. Sahoo, A.K. Arora, V. Sridharan, *J. Phys. Chem. C* 113 (2009) 16927-16933.
- [44] Y.V. Kolen'ko, K.A. Kovnir, A.I. Gavrilov, A.V. Garshev, J. Frantti, O.I. Lebedev, B.R. Churagulov, G. Van Tendeloo, M. Yoshimura, *J. Phys. Chem. B* 110 (2006) 4030-4038.
- [45] Z. Zhang, J.B.M. Goodall, S. Brown, L. Karlsson, R.J.H. Clark, J.L. Hutchison, I.U. Rehman, J.A. Darr, *Dalton Trans.* 39 (2010) 711-714.
- [46] H.Y. Zhu, Y. Lan, X.P. Gao, S.P. Ringer, Z.F. Zheng, D.Y. Song, J.C. Zhao, *J. Am. Chem. Soc.* 127 (2005) 6730-6736.
- [47] A.W. Jackson, O. Shebanova, A.L. Hector, P.F. McMillan, *J. Solid State Chem.* 179 (2006) 1383-1393.
- [48] H. Du, C.T. Williams, A.D. Ebner, J.A. Ritter, *Chem. Mater.* 22 (2010) 3519-3526.
- [49] W. You, M. Feng, Y. Zhan, R. Chen, H. Zhan, *Chemical Engineering Journal* 233 (2013) 360-368.
- [50] V. Etacheri, G. Michlits, M.K. Seery, S.J. Hinder, S.C. Pillai, *ACS Appl. Mater. Interfaces* 5 (2013) 1663-1672.
- [51] K. Kiatkittipong, A. Iwase, J. Scott, R. Amal, *Chem. Eng. Sci.* 93 (2013) 341-349.
- [52] M.-T. Nguyen-Le, B.-K. Lee, *Chem. Eng. J.* 281 (2015) 20-33.
- [53] Z. Luo, A.S. Poyraz, C.-H. Kuo, R. Miao, Y. Meng, S.-Y. Chen, T. Jiang, C. Wenos, S.L. Suib, *Chem. Mater.* 27 (2015) 6-17.
- [54] S.P. Chenakin, G. Melaet, R. Szukiewicz, N. Kruse, *J. Catal.* 312 (2014) 1-11.

- [55] S.-H. Lee, E. Yamasue, K.N. Ishihara, H. Okumura, *Appl. Catal. B* 93 (2010) 217-226.
- [56] B. Qiu, Y. Zhou, Y. Ma, X. Yang, W. Sheng, M. Xing, J. Zhang, *Sci. Rep.* 5 (2015) 8591.
- [57] R. Jaiswal, N. Patel, D.C. Kothari, A. Miotello, *Appl. Catal. B* 126 (2012) 47-54.
- [58] W. Ren, Z. Ai, F. Jia, L. Zhang, X. Fan, Z. Zou, *Appl. Catal. B* 69 (2007) 138-144.
- [59] L. Zhao, X. Chen, X. Wang, Y. Zhang, W. Wei, Y. Sun, M. Antonietti, M.-M. Titirici, *Adv. Mater.* 22 (2010) 3317-3321.
- [60] O. Rosseler, M. Sleiman, V.N. Montesinos, A. Shavorskiy, V. Keller, N. Keller, M.I. Litter, H. Bluhm, M. Salmeron, H. Destailats, *J. Phys. Chem. Lett.* 4 (2013) 536-541.
- [61] H. Irie, Y. Watanabe, K. Hashimoto, *J. Phys. Chem. B* 107 (2003) 5483-5486.
- [62] R. Asahi, T. Morikawa, T. Ohwaki, K. Aoki, Y. Taga, *Science* 293 (2001) 269-271.
- [63] D.T. Sawyer, J.M. McKinnie, *J. Am. Chem. Soc.* 82 (1960) 4191-4196.
- [64] C.-C. Wang, J.Y. Ying, *Chemistry of Materials* 11 (1999) 3113-3120.
- [65] Y. Zhang, Z.-F. Wu, P.-F. Gao, D.-Q. Fang, S.-L. Zhang, *J. Alloys Compd.* 704 (2017) 478-483.
- [66] M. Gurulakshmi, M. Selvaraj, A. Selvamani, P. Vijayan, N.R. Sasi Rekha, K. Shanthi, *Appl. Catal. A* 449 (2012) 31-46.
- [67] L.G. Devi, R. Kavitha, *Appl. Catal. B* 140–141 (2013) 559-587.

- [68] M.-T. Nguyen-Le, B.-K. Lee, RSC Adv. 6 (2016) 31347-31350.
- [69] J.-Y. Liao, B.-X. Lei, H.-Y. Chen, D.-B. Kuang, C.-Y. Su, Energy Environ. Sci. 5 (2012) 5750-5757.
- [70] M. Xi, Y. Zhang, L. Long, X. Li, J. Solid State Chem. 219 (2014) 118-126.
- [71] C. Wang, X. Zhang, Y. Zhang, Y. Jia, J. Yang, P. Sun, Y. Liu, J. Phys. Chem. C 115 (2011) 22276-22285.
- [72] B. Bhaduri, N. Verma, J. Colloid Interface Sci. 436 (2014) 218-226.
- [73] Z. Lin, A. Orlov, R.M. Lambert, M.C. Payne, J. Phys. Chem. B 109 (2005) 20948-20952.
- [74] Y. Wang, T. Sun, D. Yang, H. Liu, H. Zhang, X. Yao, H. Zhao, Phys. Chem. Chem. Phys. 14 (2012) 2333-2338.